LAWRENCE
LIVERMORE
NATIONAL
LABORATORY

UCRL-JRNL-218149

Long-term slip rate of the southern San Andreas Fault, from 10Be-26Al surface exposure dating of an offset alluvial fan

Jérôme van der Woerd, Yann Klinger, Kerry Sieh, Paul Tapponnier, F.J. Ryerson, A.-S. Mériaux

January 13, 2006

Journal of Geophysical Research - Solid Earth

Long-term slip rate of the southern San Andreas Fault, from ^{10}Be-^{26}Al surface exposure dating of an offset alluvial fan

Jérôme van der Woerd[1,2*], Yann Klinger[3,4*], Kerry Sieh[3], Paul Tapponnier[4], Frederick J. Ryerson[1], Anne-Sophie Mériaux[1,3,5*]

(1) IGPP-LLNL, L202, 7000 East Avenue, CA94550 Livermore, USA
ryerson@llnl.gov
(2) EOST-IPGS, 5 Rue R. Descartes, 67000 Strasbourg, France
jeromev@eost.u-strasbg.fr
(3) Division of Geological and Planetary Sciences 100-23, Caltech, Pasadena, CA 91125, USA
sieh@gps.caltech.edu
(4) Laboratoire de Tectonique, IPG Paris, 4 place Jussieu, 75252 Paris Cedex 05, 75252, France
klinger@ipgp.jussieu.fr
tapponnier@ipgp.jussieu.fr
(5) School of Geosciences, Institute of Geography, Drummond Street, EH8 9XP, Edinburgh, UK
meriaux1@mac.com

* Present address.

Abstract

We determine the long-term slip rate of the southern San Andreas Fault in the southeastern Indio Hills using ^{10}Be and ^{26}Al isotopes to date an offset alluvial fan surface. Field mapping complemented with topographic data, air photos and satellite images allow to precisely determine piercing points across the fault zone that are used to measure an offset of 565 ± 80 m. A total of twenty-six quartz-rich cobbles from three different fan surfaces were collected and dated. The tight cluster of nuclide concentrations from 19 samples out of 20 from the offset fan surface implies a simple exposure history, negligible prior exposure and erosion, and yield an age of 35.5 ± 2.5 ka. The long-term slip rate of the San Andreas Fault south of Biskra Palms is thus 15.9 ± 3.4 mm/yr. This rate is about 10 mm/yr slower than geological (0-14 ka) and short-term geodetic estimates for this part of the San Andreas Fault implying changes in slip rate or in faulting behavior. This result puts new constraints on the slip rate of the San Jacinto and on the Eastern California Shear Zone for the last 35 ka. Our study shows that more sites along the major faults of southern California need to be targeted to better constrain the slip-rates over different time scales.

1. Introduction

The rate of horizontal translation between the Pacific and North American plates has averaged at about 50 mm/yr over the past 3 million years [*DeMets*, 1995; *DeMets and Dixon*, 1999] and 48 ± 5 mm/yr over the past decade [*Bennett et al.*, 1996]. Many have attempted to understand how this deformation is partitioned between the numerous active faults of southern California, because such knowledge is critical to understand the mechanics of this complex plate boundary. The details of slip-rates distribution are also important input for estimating local seismic hazards, because seismic productivity generally increases with increasing fault slip rate.

Attempts to measure the partitioning of slip across the plate boundary have relied on either short- or long-term measurements. Geodetic data enable calculation of rates spanning a few years or decades; stratigraphic, geomorphologic and geochronologic information yield rate averages that span thousands to tens of thousands of years. Heretofore, measurements of long-term slip rates have been sparse, because they have depended on the presence of clearly offset landforms datable by the radiocarbon method. Only at Cajon Pass and Wallace Creek (Figure 1, inset) is the millennially averaged slip rate well constrained along the San Andreas fault (SAF) [*Weldon and Sieh*, 1985; *Sieh and Jahns*, 1984]. The rates there, 24.5 ± 3.5 and 34 ± 3 mm/yr, respectively, suggest that the fault currently bears about 50 to 70 % of the entire relative plate motion.

Use of the Cajon Pass rate to establish the nature of slip partitioning farther south in southern California is probably inappropriate, because the geometry of active faults there differs greatly from their geometry at the latitude of Cajon Creek (Figure 1, inset). South of Cajon Pass, several other active strike-slip faults lie west of and sub-parallel to the San Andreas [*Allen*, 1957]. Structural, stratigraphic and geochronologic data show that among these faults, the San Jacinto and San Andreas have long been the principal structures. Geodetic measurements show that this continues to be the case, with the two faults carrying well over half of the total relative plate motion.

The relative degree of current activity of these two faults remains controversial, however. Although the total Miocene slip across the SAF (215 km) is clearly much larger than that across the San Jacinto fault (SJF) (20 km), some interpretations suggest that the slip rate of the SJF over the past 30,000 years is equal to or greater than that of the SAF [e.g., *Merrifield et al.*, 1987; *Kendrick et al.,* 2002; *Matti and Morton*, 1993; *Bennett et al.*, 2004]. Inversion of GPS geodetic vector fields [*Bennett et al.*, 1996; *Meade and Hager,* 2005] yields best-fit slip rates of about 23-26 and 9-12 mm/yr for the southern San Andreas (SSAF) and

SJF, respectively. *Meade and Hager* [2005] allowing for more than 1 cm/yr of slip to be accommodated in the Eastern California Shear Zone (ECSZ) obtain a slow rate of 5 mm/yr for the SAF across the San Gorgonio bend north of the Indio Hills, between Cajon Pass and the Indio Hills (Figure 1).

More precise constraints on the millennially averaged slip rate of the SAF south of Cajon Pass would eliminate another degree of freedom in inversions of geodetic or structural data. Furthermore, a well-constrained slip rate would enable more realistic estimations of the average length of the seismic cycle. The current 300-year-long period of dormancy [*Sieh*, 1986; *Fumal et al.,* 2002], for example, could be an aberration from a normal, shorter interval, or it could be typical and reflect a low rate of elastic loading.

A significant hindrance to determination of well-constrained long-term slip rates has been the difficulty of dating offset surfaces. Until recently, radiocarbon dating had been the most common and reliable means for acquiring an age. Unfortunately, carbonaceous materials are rare in offset strata, and the method is limited by the short half-life of ^{14}C to features that are younger than about 50,000 years. The development of methods to date offset geomorphic surfaces by measurement of cosmic-ray produced ^{10}Be and ^{26}Al has created new possibilities for quantifying deformation in tectonically active regions [e.g., *Bierman et al.*, 1995a**;** *Ritz et al.,* 1995; *Repka et al.,* 1997; *Van der Woerd et al.,* 1998, 2002; *Zehfuss et al.,* 2001; *Mériaux et al.,* 2004, 2005; *Chevalier et al.,* 2005; *Matmon et al.,* 2005]. The value of these methods is clear from their successful application in recent studies of the kinematics of the Indian-Asian collision. Age determinations from ^{10}Be and ^{26}Al of offset alluvial fans and glacial moraines have enabled calculation of slip rates for major strike-slip faults there [*Tapponnier et al.,* 2001 and references therein]. Cosmogenic dating allows for dating of surfaces as old as about several 100,000 years and does not rely on the recovery of carbonaceous material. Here we

constrain the slip-rate along the southern SAF by measuring the age of previously undatable surfaces using ^{10}Be and ^{26}Al.

2. The Biskra Palms site

We focused our attention on an offset alluvial fan just southeast of Biskra Palms oasis, near the southeastern tip of the Indio Hills (Figure 1). For ease of reference, we will call this the Biskra Palms fan, even though it is in the drainage immediately southeast of the actual oasis. *Keller et al.* [1982] recognized that the Biskra Palms alluvial fan (Figure 2) might enable determination of a slip rate. They estimated an offset of about 700 meters, but could not find carbonaceous materials for dating the fan surface. In lieu of radiocarbon analyses, they used the degree of soil development to estimate a 20,000- to 70,000-year age of the fan surface. Their estimated slip rate was, thus, poorly constrained between 10 and 35 mm/yr, although they had reasons to favor a rate range between 23 and 35 mm/yr [*Keller et al.*, 1982].

In the following sub-sections, we will present the geology and our mapping of the site, then discuss the offsets and finally determine the age of the offsets.

2.1 Geologic setting and mapping

The Biskra Palms fan is immediately southeast of the junction of two major strands of the SAF (Figures 1 and 2). To the southeast, the SAF continues 75 km to the Salton Sea as a relatively simple, straight structure. To the northwest, the fault divides into two principal strands, the Mission Creek (MCF) and Banning (BF) faults. Offset channels and terraces between the Biskra and Thousand Palms oases indicate that the MCF is the more active of the

two near the site. The BF does not traverse the site, but becomes the principal fault farther northwest [*Allen,* 1957**;** *Keller et al.,* 1982; *Yule and Sieh,* 2003]. Near and northwest of Biskra Palms oasis, scarps demonstrate that the BF has a significant thrust component, up on the north (Indio Hills) side. Scarps also belie the existence of many secondary faults within and along the northeastern flank of the Indio Hills (Figure 2) [e.g., *Powell et al.,* 1993**;** *Clark,* 1984]. Among these faults, the Indio Hills fault, which appears to have a significant vertical component of slip. At the Biskra Palms fan, the MCF consists of two parallel strands, 400 m apart (Figure 2). Both clearly offset the alluvial fan horizontally and vertically (Figure 3). The Biskra Palms fans are fed by a small stream, nowadays intermittent, that extends about 3 km into the Indio Hills (Figure 2). The stream erodes the Ocotillo formation [*Rogers*, 1965] from a small (2.5 km^2) drainage basin. This formation contains different type of sediments from fine sandy units to coarser conglomerates providing the mostly granitic and quartzitic pebbles and cobbles found downstream on the fan surfaces.

The fan consists of a sequence of alluvial surfaces, all well preserved northwest of the modern channel until recent years (Figure 4). Quarrying operations had removed most of the younger and much of the older fan deposits by the beginning of our study in 2000 (Figure 3). Nevertheless, we were able to map the fan surfaces from old and new aerial photographs augmented by mapping in the field. To characterize the different fan surfaces and their offsets better we mapped them in the field using stereo air photos taken in both 1969 and 2004, 10-m pixel SPOT images (KJ 545-282, 13 November 1999), and SRTM digital topographic data. Several different surfaces are distinguishable on the images by the different hues that have resulted from differing degrees of development of desert pavement and varnish. The surfaces are also distinguishable by their distinct heights relative to the active streambed.

Figure 5 shows our field and remote mapping of the alluvial surfaces and faults, superimposed on the USGS 24,000-scale topographic contours and the USGS orthophoto (September 26, 1996). Cross-sections, derived from the topographic map and field mapping, display deformation of the surfaces across the fault zone and the relative heights of the terraces (Figure 5b). The cross-sections indicate a common pattern of fan agradation with slopes becoming shallower from the oldest to the youngest surface [e.g., *Van der Woerd et al.,* 2001]. Note that most of the vertical offset occurs along the southwestern strand of the MCF (SMCF) due to upslope tilting or rotation of the block separated by the SMCF and northeastern MCF (NMCF), with almost no net vertical offset of the fan surfaces across the whole fault zone (Figure 5b). Four distinct surfaces are (or were) present. From youngest to oldest, these are T0, T1, T2 and T3. Quarrying has obliterated T1 and much of the active streambed TO. T3 is clearly preserved only as a solitary remnant upstream from the fault zone, although slopes between the two fault traces may also be chaotically deformed remnants of T3. T2 is the most prominent surface and the one from which we are able to determine an offset and a slip rate. To avoid confusion, we labeled the different surfaces depending on their position upstream (u), downstream (d), or intermediate (i) when located northeast, southwest, or in between, respectively, the two MCF strands, the NMCF and the SMCF (Figure 5).

Cobbles and boulders on the T2 surface are varnished and at places embedded in pavement (Figure 6). Rounded pebbles and cobbles up to 50 cm in size are common. A discrete sublevel (T2'd) existed downstream in 1969 (Figures 4 and 5a). Unfortunately, T2'd had been completely quarried away by the time of our fieldwork. Between the two main faults, T2i is pervasively disrupted by small, oblique normal faults, oriented about 30° clockwise relative to the principal strike-slip faults [*Keller et al.,* 1982]. The normal faults crosscut abandoned drainage rills and locally offset them vertically by as much as ~10 m (Figure 5a). Only two of these faults offset the western T2 terrace riser.

The youngest abandoned surface, T1, appears clearly on the 1969-vintage stereo air photos. It is lower than T2 and less incised by secondary rills. It has a lighter tone than the T2 and T3 surfaces, probably because its bears less varnished pebbles and cobbles. Unfortunately, it had been almost totally removed by quarrying by 2000. Only a small patch of T1 remained, downstream from the fault zone (Figure 5a).

2.2 Offset measurements

Keller et al. [1982] recognized that the T2 surface has been offset by both strands of the MCF and proposed a cumulative offset of 700 m. This value appears to be an overestimate and has recently been challenged [*Dorsey,* 2002]. Thus we discuss below in some detail the nature of the piercing lines and conclude with a reassessment of the offset measurement.

From the two parallel strands of the MCF, the SMCF is the more prominent in part because its vertical offset across T2 and T3 is several tens of meters high (Figures 3, 4, 5 and 6). In detail, the fault trace consists of a set of right-stepping traces that form an arcuate zone. Several of the gullies that incise the fault scarp are offset right-laterally (Figure 5b). *Keller et al*. [1982] attributed the 50-m-high scarp to a component of reverse faulting caused by the curvature of the fault. Our observations confirm this view, and we suggest a similar interpretation on the cross-section of Figure 5b. The NMCF is more subdued and does not continue more than a couple kilometers eastward from the offset fan. To the west, it joins the main MCF strand (Figure 2). It is followed locally by an ephemeral stream course, which crosses a small playa west of T2i (Qal in *Keller et al*. [1982]). It accommodates mostly right-lateral motion (Figure 5b).

Both faults offset the western edge of T2. This is the only marker that enables us to quantify a total MCF offset precisely and accurately. In the following we describe the piercing points used to assess the total right-lateral offset of T2 (Figure 5a). First, let us consider the offset across the NMCF. North of the NMCF, the western edge of T2u is nearly linear and trends N35E (Figures 5a and 7a). For most of its length however, a younger rill has eroded the western fan margin T2u. The bed of this small channel widens downstream, toward the northern fault. On Figure 7, piercing points A and C represent the intersections with the fault of the present eastern and western edges of this widening channel. They bracket the range of plausible piercing points for T2u. Piercing point B, between these two extremes, would represent the intersection of the western edge of T2u with the fault, if the original channel edge near the fault did not deviate from its upstream trend of N35E.

South of the NMCF, the western edge of T2i consists, to the northeast, of a straight, 100-m-long, northwest facing N35E-trending scarp (Figures 4 and 5a). To the southwest the scarp bends to become N78E for 300 m and faces southeast. It clearly separates two different terraces. T3i to the northwest is represented by a chaotic surface of eroded hills, dipping on average to the northeast due to upslope tilting. T2i to the southeast is a much smoother surface, although dissected by recent small normal faults, it is less back-tilted and still dips to the southwest (Figure 5b). Several possible explanations for the existence of the northeastern western T2i fan margin may be suggested, as it may not be only the result of stream incision (Figure 5a). The fan margin may represent the largely un-eroded front of a fan delta that abutted a small lake that occupied the valley formed after tilting of T3i (Figure 5b). Fine sands and silts on the valley floor attest to the former presence of a lake (Qal in *Keller et al.* [1982]). The fan margin may be a fault scarp, due, to a reverse fault [*Keller et al.,* 1982], or to differential tilting of the T3i and T2i units as we suggest occurs between the NMCF and SMCF (Figure 5b). However, there is no field evidence that supports a faulted contact.

Whatever the actual origin of the present shape of the scarp between D and F, it is interpreted as the western margin of T2i [*Keller et al.,* 1982]. The fan margin T2i intersects the NMCF at piercing point D.

The offsets between D and A, B, and C are 90, 130 and 180 m, respectively (Figure 7a). The most likely actual offset is D-B (130 m), because in this case the upstream and downstream segments of the western edge of T2 have the same strike (Figure 5b). The two other piercing points (A and C) are probably beyond the extreme lower and upper bounds for the offset, since these yield poorly matching trends for the upstream and downstream fan edges. In actuality, the upper and lower bounds for the offset of T2 across the northern strand must be closer to B than to A and C.

We turn now to an evaluation of the offset of T2 across the SMCF. North of the SMCF, the western edge of T2i abuts a 10- to 15-m high topographic scarp (Figures 3 and 5a). Following our interpretation of the contact between T3i and T2i (see above), depending on the tilting amount of T3i when T2i was deposited, this scarp may partly or totally be a riser, reflecting incision by the T2 stream into a pre-existing ridge of T3i alluvial conglomerate. Both the riser and the edge of the T2i tread are gently arcuate and collinear with the portion of the northeastern T2i margin described above.

TheT2i riser is cut and offset right-laterally about 30 m by a minor fault that splays off of the SMCF (Figure 5a). The intersection of the T2i terrace edge and this fault are labeled E and F in Figure 7. From piercing point E the base of the terrace riser trends S78W toward the SMCF, until it is cut by another minor strand of the SMCF.

Beyond this intersection, erosion has eliminated the terrace riser. Thus, one must extrapolate to the trace of the SMCF to estimate the position of the piercing point. Linear

extrapolation to the main southern strand yields a position for the piercing point at H (Figure 7a).

This piercing point may not reflect the total offset across the SMCF, however. The arcuate nature of the riser between the NMCF and SMCF suggests that it and T2 may be right-laterally warped. The *en-échelon* field of minor faults that cuts the T2i surface also suggests that warping may have occurred (Figure 5a). However, only one of these little faults clearly offsets the terrace riser. That offset is no more than a few meters, too small to be depicted on Figure 5a. This suggests that the family of minor faults is principally a superficial feature that cuts only the thin T2i fill and not the underlying older materials. Nonetheless, these superficial faults may belie the existence of significant broad right-lateral shearing of the block between the two principal faults.

If we assume that the entire curvature of the terrace riser between the two principal fault strands is due to right-lateral warping, then we can extrapolate the N35E trend of the riser near the NMCF all the way to the SMCF to infer a piercing point at G. Since this point is about 200 m SE of piercing point H, warping could, conceivably, account for 200 m of the offset across the fault zone.

Determination of the piercing point on the southwestern side of the SMCF is less complicated. The T2 fan south of the fault has a simple geometry and is cleanly offset. Five major rills incise the fan surface south of the SMCF, including one along the fan's western margin (Figure 5a). All of these rills intersect the fault zone at a high angle and together exhibit a slightly radial pattern across the fan. These rills probably fed by the springs along the fault zone have reused or slightly widened preexisting channels at the surface of the fan surface, therefore indicating no major surface change since T2 was beheaded and abandoned.

Adjacent to the western edge of the T2d terrace is a small intermittent active stream channel. This channel is too small and services too small a drainage basin to have had the power to significantly erode the western margin of the T2d fan. Thus the current mapped edge of the T2d fan is probably within a few meters of the original fan edge. The fan edge projects N65E into the fault zone at point J (Figure 7a).

One might argue that the original fan margin and piercing point lie farther to the west and have been overridden by the thrust fault in Figure 5A. This cannot be the case, however. First, there are no young scarps that would indicate the fault has been recently active. Second, small remnants of the T2d surface present at the mouth of tributary canyons on the hanging wall block still grade to the main T2d fan.

The distance between piercing point J and piercing points H is 405 m. Addition of the 30-m offset between points E and F yields a total offset of 435 m. If we were to allow for an extreme amount of warping by matching up piercing point J and G the offset would be 600 m. (Figure 7a).

The true offset across the southern fault zone must be close to the 435-m value, because the trends of the western edges of T2 are similar in this reconstruction. The trend of the T2 fan south of the fault zone is N65E, and the trend of the T2 terrace riser immediately north of the fault zone is N78E. Even if we allow for some rotation north of the southern fault zone, by rotating the latter so that it has a N65E trend, the offset increases only by about 40-50 m. The 600-m offset, based upon 200 meters of warping, is indefensible, because it creates an enormous mismatch between the trend of the T2 terrace riser north of the fault zone and the T2 fan south of the fault. We suggest that the uncertainty in offset across the southern main fault is no more than 50 meters or so, because of the similarity in trend of the offset features north and south of the fault zone.

Figure 7b illustrates our reconstruction of offsets across the fault zone. The reconstruction assumes that no rotation has occurred. The total offset across the fault zone is 565 m, 130 m across the northern strand and 435 m across the southern strand. Allowance for enough warp to restore the trend of the T2i terrace riser to the N65E trend of the T2d fan edge increases the total offset by about 50 m, to 615 m. Offsets across the southern fault zone much smaller than 435 m [e.g., *Dorsey*, 2002] must be considered unlikely, because they require piercing lines with grossly conflicting trends. In addition, the geomorphic expression of the NMCF and SMCF are quite different implying more displacement along the southern branch. The NMCF is discontinuous and difficult to map both in the field and from air photos. The SMCF is a clear cut across the landscape, underlined with numerous springs and palm trees and at our site forms a several tens of meter high topographic scarp (Figures 3-6). It therefore appears unlikely to accumulate most of the displacement along the NMCF as implied by the interpretation of *Dorsey* [2002]. Arguments that unrecognized sinuosity in the western margin of T2 could make smaller offsets plausible are also difficult to defend. First, the western edge of the T2 surface is well preserved along most of its length, and there are no preserved abrupt changes in trend. Variations in its trend occur over hundreds, not tens of meters. Second**,** rills cut into T2 upstream and downstream support this inference, because they too tend to have rather uniform trends over short distances. The trends of the western margin of the T2 surface and the major rills cut into the T2 surface vary from N30E to N45E. If we allow this much variation in the piercing line where it has been obliterated by erosion near each of the two main fault zones, we derive an estimate of 80 m for the uncertainty in our measurement. Note that, ignoring the trend of the northwestern margin of T2i in the more chaotic zone between the two MCF strands implies to estimate an offset between piercing points B and J (Figure 7a) with varying extreme trends from N35 to N65 across the 430 m large fault zone. This would result in an average offset of 600 ± 100 m, only slightly larger than the one determined here

(Figure 7b) with a similar uncertainty. In the discussion below, we take the value of 565 ± 80 m as the best estimate of the offset of the T2 surface at the site.

2.3 Cosmogenic dating

Alluvial fan and terrace surfaces, which are abandoned streambeds, may be dated with surface exposure dating techniques if deposition and incision are events of relatively short duration. Exposure of clasts to cosmic rays before deposition on a surface (also called inheritance, [e.g., *Anderson et al.,* 1996; *Repka et al.,* 1997]) is largely a function of transport time and storage within the drainage basin. At Biskra Palms, the headwaters of the drainage basin are only 3 km away from the site of deposition. This suggests that inheritance related to exposure during transport is likely to be small [e.g., *Van der Woerd et al.,* 1998]. Exposure on eroding slopes may occur, however, and can be responsible for inherited components in the total cosmogenic nuclide content [e.g., *Anderson et al.,* 1996]. This is also the case of cobbles previously deposited and then reworked and transported into the drainage basin. To detect such potential age bias we collected multiple samples from each surface [*Bierman et al.,* 1995a**;** *Van der Woerd et al.,* 1998; 2000; 2002; *Mériaux et al.,* 2004; *Zehfuss et al.,* 2001].

Erosion is usually advocated to be the source of uncertainties in surface exposure dating [e.g., *Gosse and Phillips,* 2001]. In comparable climatic conditions, bedrock surfaces [*Bierman*, 1994; *Small et al.,* 1997; *Matmon et al.*, 2005] or large boulders [*Bierman et al.,* 1995b**;** *Phillips et al.,* 1997; *Zehfuss et al.,* 2001] have been found to erode at rates of 0,002-0.017 mm/yr and 0,002-0.004 mm/yr, respectively. We think that these rates are maximum when transposed at our site. The surface targeted here are loose conglomerates and we sampled in general cobbles (the most common rock size of the surfaces) avoiding large protruding boulders. Away from recent rills the flat fan surfaces we targeted, although they

are loosely compacted conglomerates, show no evidence of erosion, cobbles look pretty much the same as those from the present day stream bed. In general, the well-preserved cobbles showed no evidence of mass wasting due to frost or fire spalling. However, paved surfaces clearly indicate that surface weathering occurred resulting in patches of smooth surfaces. Desert pavement development and evolution is critical to assess the exposure evolution with time of the surface cobbles. Rapid development of desert pavement followed by stabilization of the surface may in fact reduce the erosion factor as a source of uncertainty [e.g., *Wells et al.,* 1995; *Quade,* 2001]. If pavements develop in relatively short times, a few centuries or a few thousand years [*Quade,* 2001], the duration of surface exposure may be close to the true age of abandonment of the surface. Hence, we consider that erosion of the samples or of the surfaces occurs at a rate slow enough to be neglected.

We dated a total of 26 quartz-rich, rooted cobbles, ranging in size from about 10 to 20 cm in diameter (Figure 6b, Table 1). Three cobbles were collected from older surfaces (two on T3u, north of the fault zone, and one on the irregular surface west of T2i; Figure 5a). From the T2 complex, we dated 20 cobbles (10 from T2u, 2 from T2i and 8 from T2d). From the youngest abandoned terrace, T1, we dated 3 cobbles (Figure 5a and Table 1). Samples locations were plotted in the field on the aerial photos, and some of them were determined with a handheld GPS. Elevation of each sample has been checked with the USGS 24,000-scale topographic contours and shielding due to surrounding relief determined for each sample (the Indio Hills crest line is the main shielding factor at the site, an horizon at about 10-15°, less than 3 km away).

We separated quartz and removed meteoric components using the chemical isolation method of *Kohl and Nishiizumi* [1992]. We separated beryllium and aluminum from the dissolved quartz by anion and cation exchange chromatography, precipitated the hydroxides and ignited them to form oxides. We measured the $^{10}Be/Be$ and $^{26}Al/Al$ ratios by accelerator

mass spectrometry (AMS) at the Lawrence Livermore National Laboratory AMS facility [*Davis et al.*, 1990]. Measurements were normalized to the ICN ^{10}Be and NBS ^{26}Al standards prepared by K. Nishiizumi (person. comm.).

In cases of negligible erosion and inheritance, model ages for ^{10}Be and ^{26}Al can be calculated from the expression

$$N(0,t) = (P_0 / \lambda)\left(1 - e^{-\lambda t}\right) \quad (1)$$

where $N(0,t)$ is the nuclide concentration at time t, P the surface production rate (atom/g/yr) and λ the decay constant of the nuclide (yr^{-1}). Zero-erosion model ages were calculated using a sea level-high latitude (SLHL) ^{10}Be production rate of 5.06 atoms/g-quartz/yr, based on measurements of glacial surfaces in the Sierra Nevada [*Nishiizumi et al.,* 1989], recalculated using the revised 13,000 yr glacial retreat ages reported by *Clark et al.* [1995], and rescaled for latitude and altitude using the coefficients of *Lal* [1991], as described in *Owen et al.* [2002]. An uncertainty of 6% on the production rate [*Stone,* 2000] is taken into account. At the latitude of our site, the variations in the geomagnetic field and pole position produce changes in the production rate. These changes can be expressed in terms of an equivalent change in geomagnetic latitude and evaluated using the data from *Ohno and Hamano* [1992], *McEllhinny and Senanayake* [1982] and the Sint-800 intensity record of *Guyodo and Valet* [1999]. For all our samples, which are at most 1.5 km apart, we use the same latitude and longitude coordinates (33.8°N, 116.2°W) and the ages were calculated using the *Stone* [2000] latitude and altitude correction factors.

The isotopic concentrations and calculated model ages appear in Table 1. For all samples, save one, both ^{10}Be and ^{26}Al measurements were performed. While for most of the samples the ratio between ^{10}Be and ^{26}Al concentrations is close to 6, we observe

systematically lower concentrations for ^{26}Al. We are more confident in the ^{10}Be ages because they rely on a single ratio measurement, whereas the ^{26}Al determination requires two measurements, the $^{26}Al/^{27}Al$ ratio and the ^{27}Al concentration. For these reasons, we use only the ^{10}Be data in the final age calculations, which include the geomagnetic correction (Table 1). As such, these ages are calibrated and can be compared to dates derived from other dating methods (calibrated radiocarbon dating, for example).

South of the main fault (Figure 5a), 8 samples from T2d yield ages of 33 to 37 ka. The averaged value of these ages is 35.4 ± 1.4, with no outliers (Figure 8). The 3 samples from T1 yield ages ranging from 11 to 37 ka (Figure 8). Since T1 cannot be older than T2, the oldest sample could be a reworked cobble from T2. The average age of the two youngest samples of T1, 14 ± 4 ka, is our best estimate of the age of this surface.

Between the two main faults, the average of the two cobble exposure ages obtained for T2i (33.8 and 37.1 ka) is 35.4, in good agreement with the average age of cobbles on T2d. The age of the one sample from the surface west of T2i (38.4 ka) is only slightly greater than the average age of T2.

North of the faults we sampled two surfaces, T2u and T3u. Nine of the 10 samples from T2u yield ages between 31 and 40 ka, average 37.4 ± 4.4 ka, in keeping with the ages on T2i and T2d. But one sample is significantly older (45.8 ka). The two samples from T3u have ages comparable to that of T2u, even though this terrace level stands several meters higher than T2.

In summary, the age of T2 is well constrained, by 19 sample ages that cluster tightly and yield an average age of 35.5 ± 2.5 ka (Figure 8 and Table 1). The 45 Ka age of one sample from T2u is clearly an outlier and probably indicates reworking of a previously

exposed clast. T1 (~14 ka) is at least 20 ka younger than T2, and might be as young as 11 ka. The age of T1 indicates emplacement of T1 after the end of the Last Glacial Maximum.

3. Long-term slip rate

We may conclude confidently that the T2 surface was emplaced 35.5 ± 2.5 kyr ago. Subsequent to that date of deposition, the surface has been offset 565 ± 80 m. Dividing this offset by this age yields an average slip rate of 15.9 ± 3.4 mm/yr at the Biskra Palms fan. This rate is lower than the geological rates determined to the north along the SAF at Cajon Pass (24.5 ± 3.5 mm/yr, *Weldon and Sieh*, [1985]). However, as discussed below, the rate calculated here may be considered a minimum bound.

In any case, it is presently the only and best direct estimate of the rate of right-lateral displacement on the main branch of the SAF across the Indio Hills. Despite fault related deformation along the two main fault branches the reconstruction of the geometry of the northwestern limit of T2 we propose is realistic. Conservatively, we have considered a simple, almost linear, shape for this limit (Figure 7b) in agreement with the present day geomorphic characters of the surface suggested both from topographic contours and post-depositional rill incisions. Such characters require that the total offset of the T2 limit, mapped on figure 5a, must have accrued after the T2 conglomeratic fan was abandoned. Because of overlapping fan deposits downstream of the fault coupled with a component of thrusting (Figure 5a), the southeastern limit of T2 is less well defined, but overall the total offset is unlikely to be less than 500 m.

The abandonment age of T2 (35.5 ± 2.5 ka), determined from sets of samples from various parts of the surface upstream and downstream from the two fault-strands yields strong

constraints on the age of the total offset of T2. The large number of surface samples (a total of 19, Figures 5a and 8), distributed over large areas of the three T2 remnants, with well clustered ages, confirm that pre-depositional exposure or post-depositional erosion were negligible and that the 35.5 ± 2.5 ka age is statistically representative of the timing of abandonment of T2. In addition, this age, which is calibrated and integrates topographic and geomagnetic corrections, corresponds to a well-known interstadial at 35 ka, a warm pluvial separating Marine Isotope Stages 3 and 2, also described in lake sediments at Owens Lake [e.g., *Bischoff and Cummins*, 2001] and Mono Lake [*La Joie*, 1968]. This would have been a period propitious to fan aggradation and fairly rapid abandonment.

While the rate we find is low, we argue that it is a minimum bound for the total slip-rate across the entire fault zone at Biskra Palms. As shown above, there is additional faulting and deformation at the site that is difficult to assess quantitatively. In particular, there are numerous N160-170 trending normal faults [*Keller et al.*, 1982] visible across T2 and between the two major strike-slip faults (Figure 5a). A few of these faults have dextral offsets of several meters. They probably accommodate internal deformation of the block between the main faults and ought to be responsible for additional right lateral slip at the site. While motion on these faults might attest to counter-clockwise rotation of the small blocks they separate, clockwise rotation of the entire block between the two major strike-slip faults may also occur. A rotation of only 7° of this 400 m wide block would add up to 50 m to the total right-lateral offset and would increase the slip-rate by more than 10 %. Furthermore, as shown on figures 1 and 2, faults north of the most prominent strands may accommodate additional right-lateral motion in the Indio Hills. They might easily account for another 10 % increase in the slip-rate.

The major problem at Biskra Palms is to assess how the BF connects to the MCF and where. Clearly, the BF accommodates most of the right-lateral motion of the SAF as one

moves 15 km northwest of the Indio Hills. The slip-transfer must occur within the Indio Hills, but is probably not complete at Biskra Palms. The BF becomes less and less clear as it approaches its southeastern termination, with stepping *en-échelons* segments that have a thrust component (Figure 2), responsible for uplift and upslope tilting of the hills southwest of the MCF. Such uplift terminates at Biskra Palms, as evidenced by the disappearance of the hills immediately to the southeast, and no additional faulting is observed across the fans farther south.

Therefore, the actual rate could reach a value closer to that determined at Cajon Pass, north of the San Gorgonio bend along the main trace of the San Andreas fault. Such a rate would be in keeping with recent geodetic (GPS or VLBI) data that estimate the rate along the MCF to range between 21 and 28 mm/yr [*Feigl et al.,* 1993; *Bennett et al.,* 1996]. Note that the highest rate estimate is provided by the GPS data (26 ± 2 mm/yr, [*Bennett et al.,* 1996]), which integrates strain over a wide area, with the eastern most stable points being as far as 100 km away from the SAF [*Bennett et al.,* 1996]. If a few mm/yr of strain is taken up east of the Indio Hills then a better agreement between our rate and the GPS data ensues.

Alternatively, the slip-rate along the SAF from Cajon Pass to the Indio Hills might not be constant and a decrease in slip could be envisaged as the fault crosses the San Gorgonio bend [e.g., *McGill et al.,* 2002], and could decrease even more towards Salton Sea [e.g., *Shifflett et al.,* 2002; *Sieh and Williams*, 1990]. If this were the case, then some form of distributed strain transfer might occur among the different faults that make up the plate boundary. In particular, the San Jacinto Fault (SJF) might become faster and could take up as much as 10-15 mm/yr of slip, in agreement with the fastest slip estimate along it [e.g., *Sharp,* 1981; *Merrifield et al.,* 1987; *Rockwell et al.,* 1990**;** *Bennett et al.,* 2004; *Kendrick et al.,* 2002; *Anderson et al.,* 2003; *Becker et al.,* 2005].

To further assess the validity of our rate within the broader, regional active deformation framework, we show on Figure 9 the rates of slip on most of the faults across southern California. The rates compiled are from a variety of sources and were determined by different methods (Table 2) [e.g., *Wesnousky*, 1986; *Peterson and Wesnousky*, 1994; *Jennings*, 1994; *Dokka and Travis,* 1990; *McGill and Sieh*, 1993; *Lee et al.,* 2001; *Salyards et al.,* 1992; *Williams,* 1989]. When possible we show geologically determined rates, which provide information over comparable time spans. Considering the total slip budget across the plate boundary along three different paths (1-3, Figure 9), we obtain similar values of about 40-51 mm/yr. This first order calculation likely underestimates the total motion of the Pacific plate relative to North America, which probably explains the difference with the Nuvel-1A predictions of 45-55 mm/yr ([*Demets*, 1995; *DeMets and Dixon*, 1999], Figure 9). If one considers that the total rates across the three paths have to be the same, we may infer the rates across other faults of the plate boundary. Either the SJF moves fast, up to 20 mm/yr, (path 3B in Figure 9), i.e. 40 % of the plate motion [e.g., *Kendrick et al.,* 2002]. Or, the SJF moves at 12 mm/yr and up to 1 cm/yr is already accommodated towards the northeast, in the ECSZ, (path 3A in Figure 9), [e.g., *Meade and Hager*, 2005].

4. Conclusion

The slip rate we obtain at Biskra Palms using cosmogenic dating (15.9 ± 3.4 mm/yr) spans a 35,000 years period, and places a strong new constraint on slip distribution amongst the faults of southern California.

To a first order, this rate is slower than even the lower bounds of the geological rate at Cajon Pass, 24.5 ± 3.5 mm/yr [*Weldon and Sieh*, 1985], and of the VLBI [*Feigl et al*., 1993]

and GPS [*Bennett et al*., 1996; *Meade and Hager,* 2005] rates of 26 ± 2 mm/yr and 23 ± 2 mm/yr, respectively. Yet, it confirms that near Indio, the MCF is the principal strand of the SAF, accommodating most (35%) of the relative motion between the Pacific and North American plates. The relatively slow rate on the main branch of the SAF at Biskra Palms suggests that the slip rate on the San Jacinto Fault maybe closer to the upper bounds of rates determined along this fault (12-20 mm/yr). Because it remains on the low side of all other rates determined on the southern SAF, we suspect that it is a minimum bound. This inference is supported by the fact that we obtain this rate at a rather complex location where the SAF splits into two branches (BF and MCF), with a significant change in strike (~10° towards west). Some motion must be accommodated by thrusting at Biskra Palms, and probably some more by adjacent normal faults. Also, the rates at Cajon Pass and Biskra, on either side of the San Gorgonio restraining bend, need not be precisely the same, if diffuse strain transfer occurs across the San Bernardino and San Jacinto mountains [e.g., *Spotila et al.*, 1998; *Kendrick et al*., 2002). Finally, space geodesy rates span only the last 15 years and, as observed elsewhere [e.g., *Peltzer et al*., 2001], millennial slip rates, especially spanning as much as 35,000 years, need not be identical if strain build-up varies through the seismic cycle and on larger time-scales [*Bennett et al*., 2004; *Friedrich et al.*, 2003; *Dixon et al.,* 2003].

Acknowledgments

We like to thank Granite Corporation for allowing unlimited access to the fans, and especially to Lola Green and Lilburn Corporation for sharing topographic data. Tom Rockwell was kind enough to take one of us in his plane to fly over the Indio Hills. We thank S. Mitchell and B. Dorsey for their critical reviews and comments that improved the final version of the manuscript. We thank R.C. Finkel and M.W. Caffee at Lawrence Livermore National Laboratory for their help in analyzing the samples. The Lawrence Livermore National Laboratory (LLNL) group acknowledges support from the Laboratory Directed Research and Development Program at LLNL, operating under the auspices of the U.S. Department of Energy contract No. W-7405-Eng-48. This research was supported in part by the Gordon and Betty Moore Foundation. This is Caltech Tectonic Observatory Contribution #9.

References

Allen, C.R. (1957), San Andreas fault zone in San Gorgonio Pass, southern California, *Bull. Geol. Soc. Am., 68*, 315-350.

Anderson G., D.C. Agnew, and H.O. Johnson (2003), Salton Trough regional deformation estimated from combined trilateration and survey-mode GPS data, *Bull. Seismol. Soc. Am., 93,* 2402-2414.

Anderson, R.S., J.L. Repka and G.S. Dick (1996), Explicit treatment of inheritance in dating depositional surfaces using in situ ^{10}Be and ^{26}Al, *Geology*, *24*, 47-51.

Becker, T.W., J.L. Hardebeck, and G. Anderson (2005), Constraints on fault slip rates of the southern California plate boundary from GPS velocity and stress inversions, *Geophys. J. Int., 160,* 634-650, doi: 10.1111/j.1365-246X.2004.02528.x.

Bennett, R.A., W. Rodi, and R.E. Reilinger (1996), Global Positioning System constraints on fault slip rates in southern California and northern Baja, Mexico, *J. Geophys. Res.*, *101*, 21,943-21,960.

Bennett, R.A., A.M. Friedrich, and K.P. Furlong (2004), Codependent histories of the San Andreas and San Jacinto fault zones from inversion of fault displacement rates, *Geology*, *32*, 961-964, doi: 10.1130/G20806.1.

Bierman, P.R. (1994), Using in situ cosmogenic isotopes to estimate rates of landscape evolution: A review from the geomorphic perspective, *J. Geophys. Res.*, *99*, 13,885-13,896, doi:10.1029/94JB00459.

Bierman, P.R., A.R. Gillespie, and M.W. Caffee (1995a), Cosmogenic ages for earthquake recurrence interval and debris flow fan deposition, Owens Valley, California, *Science*, *270*, 447-450.

Bierman, P.R., A.R. Gillespie, M.W. Caffee, and D. Elmore (1995b), Estimating erosion rates and exposure ages with ^{36}Cl produced by neutron activation, *Geochem. Cosm. Acta, 59*, 3779-3798.

Bischoff, J.L., and K. Cummins (2001), Wisconsin glaciation of the Sierra Nevada (79,000-15,000 yr B.P.) as recorded by rock flour in sediments of Owens Lake, California, *Quaternary Research*, *55*, 14-24.

Chevalier, M.L., F.J. Ryerson, P. Tapponnier, R.C. Finkel, J. Van der Woerd, Li H., and Liu Q. (2005), Slip-rate measurements on the Karakorum fault may imply secular variations in fault motion, *Science*, *307*, 411-414.

Clark, M.M. (1984), Map showing recently active breaks along the San Andreas fault and associated faults between Salton Sea and Whitewater River-Mission Creek, California, U.S. Geological Survey Miscellaneous Investigations Map I-1483, scale 1:24,000.

Clark, D.H., P.R. Bierman, and P. Larsen (1995), Improving in-situ cosmogenic chronometers, *Quaternary Research*, *44*, 367-377.

Davis, J.C., I.D. Proctor, J.R. Southon, M.W. Caffee, D.W. Heikkinen, M.L. Roberts, K.W. Turteltaub, D.E. Nelson, D.H. Loyd, and J.S. Vogel (1990), LLNL/UC AMS facility and research program: Nuclear instruments and methods in Physics Research, *B52*, 269-272.

DeMets, C. (1995), Reappraisal of seafloor spreading lineations in the Gulf of California: Implications for the transfer of Baja California to the Pacific plate and estimates of Pacific-North America motion, *Geophys. Res. Lett., 22*, 3545-3548.

DeMets, C., and T. H. Dixon (1999), New kinematic models for Pacific-North America motion from 3 Ma to present, I: Evidence for steady motion and biases in the NUVEL-1A model, *Geophys. Res. Lett., 26,* 1921-1924.

Dixon, T.H., E. Norabuena, and L. Hotaling (2003), Paleoseismology and Global Positionning System: Earthquake cycle effects and geodetic versus geologic fault slip rates in the Eastern California shear zone, *Geology, 31*, 55-58.

Dokka, R.K., and C.J. Travis (1990), Late Cenozoic strike-slip faulting in the Mojave desert, California, *Tectonics*, *9*, 311–340.

Dorsey, B. (2002), Late Pleistocene slip-rate on the Coachella Valley segment of the San Andreas fault and implications for regional slip partitioning, abstract, Cordilleran Section GSA 99th Annual Meeting, April 1-3, 2003, Puerto Vallarta, Jalisco, Mexico.

Feigl, K.L. *et al*. (2003), Space geodetic measurement of crustal deformation in central and southern California, 1984-1992, *J. Geophys. Res., 98,* 21,677-21,712.

Friedrich, A.M., B.P. Wernicke, N.A. Niemi, R.A. Bennett, and J.L. Davis (2003), Comparison of geodetic and geologic data from the Wasatch region, Utah, and

implications for the spectral character of Earth deformation at periods of 10 to 10 million years, *J. Geophys. Res., 108 (B4)*, 2199, doi:10.1029/2001JB000682.

Fumal, T.E., M.J. Rymer, and G.G. Seitz (2002), Timing of large earthquakes since AD 800 on the Mission Creek strand of the San Andreas fault zone at Thousand Palms Oasis, near Palm Springs, California, *Bull. Seism. Soc. Am., 92,* 2841-2860.

Gosse, J.C., and F.M. Phillips (2001), Terrestrial in situ cosmogenic nuclides: Theory and application, *Quat. Sci. Rev.,* 20, 1475-1560, doi: 10.1016/S0277-3791(00)00171-2.

Guyodo, Y., and J.P. Valet (1999), Global changes in intensity of the Earth's magnetic field during the past 800 kyr, *Nature, 399*, 249-252.

Hart, E.W., W.A. Bryant, C.J. Wills, J.A. Treiman, and J.E. Kahle (1989), Summary Report: Fault Evaluation Program, 1987-1988, Southwestern Basin and Range Region and Supplemental Areas. Depart of Conservation, Division of Mines and Geology Open-File Report 89-16.

Jennings, C.W. (1994), Fault Activity Map of California and Adjacent Areas with Location and Ages of Recent Volcanic Eruptions. California Geologic Data Map Series, Map No. 6. California Division of Mines and Geology.

Keller, E.A., M.S. Bonkowski, R.J. Korsch, and R.J. Shlemon (1982), Tectonic geomorphology of the San Andreas fault zone in the southern Indio Hills, Coachella Valley, California, *Geol. Soc. Am. Bull., 93*, 46-56.

Kendrick, K.J., D.M. Morton, S.G. Wells, and R.W. Simpson (2002), Spatial and temporal deformation along the northern San Jacinto fault, southern California: Implications for slip rates, *Bull. Seism. Soc. Am., 92*, 2782-2802.

Kohl, C.P., and K. Nishiizumi (1992), Chemical isolation of quartz for measurement of in-situ produced cosmogenic nuclides, *Geochim. Cosmochim. Acta*, *56*, 3583-3587.

LaJoie, K.R. (1968), Quaternary stratigraphy and geologic history of Mono Basin, Eastern California, thesis, Ph.D., Department of Geology and Geophysics, University of California, Berkeley, California, USA.

Lal, D. (1991), Cosmic ray labeling of erosion surfaces: In situ production rates and erosion models, *Earth Planet. Sci. Lett.*, *104*, 424-439.

Lee, J., J. Spencer, and L. Owen (2001), Holocene slip rates along the Owens Valley fault, California: implications for the recent evolution of the Eastern California Shear Zone, *Geology, 29,* 819-822.

Matti, J.C., and D.M. Morton (1993), Paleogeographic evolution of the San Andreas fault in southern California: A reconstruction based on a new cross-fault correlation, in *The San Andreas Fault System: Displacement, Palinspastic Reconstruction, and Geologic Evolution*, Powell, R.E., Weldon, R.J., and Matti, J.C., eds., *Geol. Soc. Am. Memoir, 178*, 107-159.

Matmon, A., D.P. Schwartz, R. Finkel, S. Clemmens, and T. Hanks (2005), Dating offset fans along the Mojave section of the San Andreas fault using cosmogenic ^{26}Al and ^{10}Be, *Geol. Soc. Am. Bull., 117*, 795-807, doi:10.1130/B25590.

McElhinny, M.W., and W.E. Senanayake (1982), Variations in the geomagnetic dipole 1: the past 50,000 years, *J. Geomag. Geoelec.*, *34*, 39-51.

McGill, S., and K. Sieh (1993), Holocene slip rate of the central Garlock Fault in southeastern Searles valley, California, *J. Geophys. Res.*, *98*, 14,217-14,231.

McGill, S., S. Derham, K. Barton, T. Berney-Ficklin, D. Grant, C. Hartling, K. Hobart, R. Minnich, M. Rodriguez, E. Runnerstrom, J. Russell, K. Schmoker, M. Stumfall, J. Townsend, and J. Williams (2002), Paleoseismology of the San Andreas fault at Plunge Creek, near San Bernardino, southern California, *Bull. Seimol. Soc. Am., 92*, 2803-2840.

Meade, B.J., and B.H. Hager (2005), Block models of crustal motion in southern California constrained by GPS measurements, *J. Geophys. Res.*, *110*, B03403, doi: 10.1029/2004JB003209.

Mériaux, A.-S., F.J. Ryerson, P. Tapponnier, J. Van der Woerd, R.C. Finkel, Xu X., Xu Z., and M.W. Caffee (2004), Rapid slip along the central Altyn Tagh Fault: Morphochronologic evidence from Cherchen He and Sulamu Tagh, *J. Geophys. Res., 109* (B6): art. no.-B06401.

Mériaux, A.-S., P. Tapponnier, F.J. Ryerson, Xu X., G. King, J. Van der Woerd, R.C. Finkel, Li H., M.W. Caffee, Xu Z., and Chen W. (2005), The Aksay segment of the northern Altyn Tagh fault: tectonic geomorphology, landscape evolution, and Holocene slip rate, *J. Geophys. Res., 110*, B04404, doi:10.1029/2004JB003210.

Merrifield, P.M., T.K. Rockwell, and C.C. Loughman (1987), Slip rate on the San Jacinto fault zone in the Anza seismic gap, southern California, *Geol. Soc. of Am. Abst. with Progs.*, *19*, 431.

Nishiizumi, K., E.L. Winterer, C.P. Kohl, J. Klein, R. Middleton, D. Lal, and J.R. Arnold (1989), Cosmic ray production rates of ^{10}Be and ^{26}Al in quartz from glacially polished rocks, *J. Geophys. Res., 94 (B12),* 17907-17915.

Ohno, M., and Y. Hamano (1992), Geomagnetic poles over the past 10,000 years, *Geophys. Res. Lett.*, *19*, 1715-1718.

Owen, L.A., R.C. Finkel, M.W. Caffee, and L. Gualtieri (2002), Timing of multiple glaciations during the Late Quaternary in the Hunza Valley, Karakoram Mountains, Northern Pakistan: defined by cosmogenic radionuclide dating of moraines, *Geol. Soc. Am. Bull., 114*, 5, 593-604.

Peltzer, G., F. Crampe, S. Hensley, and P. Rosen (2001), Transient strain accumulation and fault interaction in the Eastern California shear zone, *Geology*, *29*, 975-978.

Petersen, M.D., and S.G. Wesnousky (1994), Fault slip rates and earthquake histories for active faults in southern California, *Bull. Seismol. Soc. Am.*, *84*, 1608-1649.

Phillips, F.M., M.G. Zreda, J.C. Gosse, J. Klein, E.B. Evenson, R.D. Hall, O.A. Chadwick, and P. Sharma (1997), Cosmogenic ^{36}Cl and ^{10}Be ages of Quaternary glacial and fluvial deposits of the Wind River Range, Whyoming, *Geol. Soc. Am. Bull.*, *109*(11), 1453-1463.

Powel, R.E., R.J. Weldon, and J.C. Matti (1993), The San Andreas Fault system: Displacement, palinspastic reconstruction, and geologic evolution, *Geol. Soc. Am. Memoir*, *178*, 332p.

Quade, J. (2001), Desert pavements and associated rock varnish in the Mojave Desert: How old can they be ?, *Geology,* 29, 855-858.

Repka, J.L., R.S. Anderson, and R.C. Finkel (1997), Cosmogenic dating of fluvial terraces, Fremont River, Utah, *Earth Planet. Sci. Lett.*, *152*, 59-73.

Ritz, J.F., E.T. Brown, D.L. Bourlès, H. Phillip, A. Schlupp, V.M. Raisbeck, F. You and B. Enkhtuvshin (1995), Slip rates along active faults estimated with cosmic-ray-exposure dates: Application to the Bogd fault, Gobi-Altaï, Mongolia, *Geology*, *23*, 1019-1022.

Rockwell , T., C. Loughman, and P. Merrifield (1990), Late Quaternary rate of slip along the San Jacinto fault zone near Anza, Southern California, *J. Geophys. Res.*, *95*, 8593-8605.

Rogers, T.H. (1965), Geologic Map of California, Santa Ana Sheet, fifth printing 1985, Olaf P. Jenkins edition, California Division of Mines and Geology.

Salyards, S.L., K.E. Sieh, and J.L. Kirschvink (1992), Paleomagnetic measurements of non-brittle deformation across the San Andreas fault at Pallett Creek, *J. Geophys. Res.*, *97*, 12,457–12,470.

Sharp, R.V. (1981), Variables rates of late Quaternary strike-slip on the San Jacinto fault zone, southern California, *J. Geophys. Res.*, *86*, 1754-1762.

Shifflet, H., M.G. Gray, R. Grannell, and B. Lynn Ingram (2002), New evidence on the slip rate, renewal time, and late Holocene surface displacement, southernmost San Andreas fault, Mecca Hills, California, *Bull. Seimol. Soc. Am., 92,* 2861-2877.

Sieh, K., and R. Jahns (1984), Holocene activity of the San Andreas fault at Wallace Creek, California, *Geol. Soc. Am. Bull, 95*, 883-896.

Sieh, K. (1986), Slip rate across the San Andreas fault and prehistoric earthquakes at Indio, California, *Eos Trans. AGU*, *67*, 1200.

Sieh, K.E., and P.L. Williams (1990), Behavior of the southernmost San Andreas fault during the past 300 years, *J. Geophys. Res., 95*, 6629-6645.

Small, E.E., R.S. Anderson, J.L. Repka, and R.C. Finkel (1997), Erosion rates of alpine bedrock summit surfaces deduced from in situ ^{10}Be and ^{26}Al, *Earth Planet. Sci. Lett., 150*, 413-425.

Spotila, J.A., K.A. Farley, and K. Sieh (1998), Uplift and erosion of the San Bernardino Mountains associated with transpression along the San Andreas fault, California, as constrained by radiogenic helium thermochronometry, *Tectonics*, *17*, 360-37.

Stone, J.O. (2000), Air pressure and cosmogenic isotope production, *J. Geophys. Res.*, *105*, 23,753-23,759.

Tapponnier, P., F.J. Ryerson, J. Van der Woerd, A.-S. Mériaux, and C. Lasserre (2001), Long-term slip rates and characteristic slip: keys to active fault behaviour and earthquake hazard, *C. R. Acad. Sci., Ser. II, 333*(9), 483–494.

Thomas, A.P., and T.K. Rockwell (1996), A 300- to 550-year history of slip on the Imperial fault near the U.S.-Mexico border: Missing slip at the Imperial fault bottleneck, *J. Geophys. Res., 101*(B3), 5987-5998, doi: 95JB01547.

Van der Woerd, J., F.J. Ryerson, P. Tapponnier, Y. Gaudemer, R. Finkel, A.S. Mériaux, M. Caffee, Zhao G., and He Q. (1998), Holocene left slip-rate determined by cosmogenic

surface dating on the Xidatan segment of the Kunlun Fault (Qinghai, China), *Geology*, *26*, 695-698.

Van Der Woerd J., F.J. Ryerson, P. Tapponnier, A.S. Mériaux, Y. Gaudemer, B. Meyer, R.C. Finkel, M.W. Caffee, Zhao G., Xu Z. (2000), Uniform slip-rate along the Kunlun Fault: implications for seismic behaviour and large-scale tectonics, *Geophys. Res. Lett.*, *27*, 2353-2356.

Van Der Woerd J., Xu X., Li H., P. Tapponnier, B. Meyer, F.J. Ryerson, A.S. Mériaux, Xu Z. (2001), Rapid active thrusting along the northwestern rangefront of the Tanghenan Shan (Western Gansu, China), *J. Geophys. Res., 106*, 30,475-30,504.

Van der Woerd, J., P. Tapponnier, F.J. Ryerson, A.S. Mériaux, B. Meyer, Y. Gaudemer, R.C. Finkel, M.W. Caffee, Zhao G., and Xu Z. (2002), Uniform postglacial slip-rate along the central 600 km of the Kunlun Fault (Tibet), from ^{26}Al, ^{10}Be and ^{14}C dating of riser offsets, and climatic origin of the regional morphology, *Geophys. J. Int*, *148*, 356-388.

Weldon, R.J., and K.E. Sieh (1985), Holocene rate of slip and tentative recurrence interval for large earthquakes on the San Andreas fault, Cajon Pass, southern California, *Geol. Soc. Am. Bull.*, *96*, 793-812.

Weldon. R.J., and E. Humphreys (1986), A kinematic model of southern California, *Tectonics, 5*, 33-48.

Wells, S.G., L.D. McFadden, J. Poths, and C.T. Olinger (1995), Cosmogenic ^{3}He surface-exposure dating of stone pavements: Implications for landscape evolution of deserts, *Geology, 23*, 613-616.

Wesnousky, S.G. (1986), Earthquakes, Quaternary faults, and seismic hazards in California, *J. Geophys. Res.*, *91*, 12,587-12,631.

Williams, P.L. (1989), Aspects of the earthquake geology and seismotectonics of the southern San Andreas and relatd fault, southern California, Thesis, Ph.D., Columbia University, New York, USA.

Yule, D., and K. Sieh (2003), Complexities of the San Andreas fault near San Gorgonio Pass: Implications for large earthquakes, *J. Geophys. Res.*, *108*, 2548, doi:10.1029/2001JB000451.

Zehfuss, P.H., P.R. Bierman, A.R. Gillespie, R.M. Burke and M.W. Caffee (2001), Slip rates on the Fish Spring fault, Owens Valley, California, deduced from cosmogenic ^{10}Be and ^{26}Al and soil development on fan surfaces, *Geol. Soc. Am. Bull., 113*, 241-255.

Table 1. ^{10}Be and ^{26}Al nuclide concentrations for 26 surface samples from different alluvial surfaces at Biskra Palms site. ^{10}Be age is calculated with corresponding geographic and topographic correction factors (see text for details). Average age and standard deviation are calculated for each surface. Star indicates sample not included in average calculation.

Table 2. Slip-rates along the faults of southern California referred to in text and plotted in Figure 9.

Figure captions

Figure 1: Map of San Andreas Fault system in the Coachella Valley. Fault map in eastern Indio Hills modified from *Clark* [1984]. Biskra Palms site is located along southwestern Indio Hills, just southeast of the Biskra Palms oasis. Background is shaded DEM derived from Shuttle Radar Topography Mission data (30m pixel). Inset, modified from *Weldon and Humphreys* [1986], shows Biskra Palms site in relation to other sites where geological long-term slip-rate have been already determined. Gray arrows [*Weldon and Humphreys*, 1986] indicate relative motion of various crustal blocks relative to North American plate (SCF: San Clemente Fault; EF: Elsinore Fault; SJF: San Jacinto Fault; SAF: San Andreas Fault; GF: Garlock Fault; PMF: Pinto Mountain Fault; SG: San Gorgonio Pass fault zone; SJ: San Jose; LA: Los Angeles; SD: San Diego).

Figure 2: a) SPOT image (KJ 545-282, 13 November 1999) of the southeastern Indio Hills. Main trace of San Andreas fault is visible across uplifted and dissected alluvial sands and gravels of the Indio Hills. Streams that cross the main fault trace have jogs that are characteristic of right-lateral motion along the fault. b) Interpretation of SPOT image outlining main strands of San Andreas fault and faults across Indio Hills (modified from *Clark* [1984]).

Figure 3: Oblique aerial view of the Biskra Palms fan surface, offset by two strands of the Mission Creek fault. By the time the photo was taken, in 2002, most of the fan downstream from the principal strand of the fault had been removed by quarrying. White arrows are piercing points of offset fan surface (dark gray) across two strands of San Andreas fault.

Figure 4: Vertical aerial photo of Biskra Palms site (May 6, 1969). Main fan surface T2d, south of the fault, has been disconnected from its upstream counterparts T2i and T2u, by right-lateral motion along the fault. Youngest alluvial surfaces are T0. T1d is an intermediate terrace.

Figure 5: a) Map of fault traces and alluvial surfaces superimposed on topographic contours and USGS orthophoto (26 September 1996). Numbered dots show locations of samples collected for cosmogenic dating. Straight lines indicate positions of topographic profiles plotted in Figure 5b. b) Superimposed topographic profiles across main alluvial levels, projected to a line perpendicular to strike of the fault zone. Match between surfaces northeast and southwest of central fault zone is clear. Main scarp along the principal strike-slip fault is likely due to thrust component and uplift of block between the two strike-slip faults. Fault geometry at depth, though hypothetical, is consistent with this interpretation.

Figure 6: a) The surface of terrace T2d, downstream of the fault zone. View to northeast, towards principal fault zone marked by aligned palm trees and by scarp. Lightly varnished cobbles paving the alluvial surface are typical of those sampled for surface exposure dating. b) Close-up of desert pavement on T2u surface northeast of fault. The white cobble near the head of the rock hammer is sample #18 (^{10}Be age of 35.4 ± 3.9 ka).

Figure 7: a) Map of alluvial unit T2, faults and various considered piercing points. Small white dots are points surveyed in the field along piercing lines. Dashed lines are western edges of T2 that we consider for offset estimation. Lettered circles are piercing points defined by intersection of dotted lines with fault traces. b) Preferred reconstruction of T2 surface and corresponding total offset values.

Figure 8: Plot of ^{10}Be model ages for each surface. The positions of each principal fault strand relative to the surfaces appear as vertical lines. Dotted line represents average age for T2. Light grey stripe is average standard deviation for samples represented by squares. Data are tabulated in Table 1.

Figure 9: a) Map of Southern California active faults. Values for slip-rates on various faults and sites along SAF are from the literature (Table 2). Rates are expressed for right-lateral slip in mm/yr, except for GFZ and PMF, which are left-lateral faults. New rate at Biskra Palms is from this study. Dotted lines 1, 2 and 3 are paths along which we summed slip-rates across plate boundary. WC: Wallace Creek; PC: Palett Creek; CP: Cajon Pass; OVFZ: Owens Valley Fault Zone; PVFZ: Panamint Valley Fault Zone; DVFZ: Death Valley Fault Zone; BF: Blackwater Fault; BUF: Bullion Fault; CFZ: Calico Fault Zone; EMF: Emerson Fault; PMF: Pinto Mountain Fault; SGP: San Gorgonio Pass; IFZ: Imperial Fault Zone; CPF: Cerro Prieto Fault; SJF: San Jacinto Fault; EF: Elsinore Fault; NIFZ: Newport-Inglewood Fault Zone; CBFZ: Coronado Bank Fault Zone; SDTFZ: San DiegoTrough Fault Zone; SCF: San Clemente Fault. b) Total slip of Pacific-America plate boundary for paths 1, 2 and 3 shown in Figure 9a. Considering an average plate boundary rate of 48-50 mm/yr (thick gray dotted line), the rate found in this study implies that either slip transfer (5-10 mm/yr) occurs towards

the Eastern California Shear Zone east of our site (path 3A) or that the SJF is fast (> 20 mm/yr; path 3B).

Table 1. ^{10}Be and ^{26}Al nuclide concentration for 26 surface samples of different alluvial surfaces at the Biskra Palms site.

Sample number	Elevation (m a.s.l.)	^{10}Be 10e4 at.g-1	^{26}Al 10e4 at.g-1	^{26}Al/^{10}Be	lat/alt correction	depth/top correction	^{10}Be age	Mean terrace Age§ (years)
Terrace T3u								
9	170	14.544 ± 2.079	87.769 ± 11.783	6.03	1.0076	0.9549	30.7 ± 4.47	
10	170	17.169 ± 2.001	80.138 ± 9.414	4.67	1.0076	0.9549	35.96 ± 4.31	**33.33 ± 3.72**
Terrace T2u								
13	165	19.026 ± 1.892	87.789 ± 11.432	4.61	1.0034	0.9550	39.66 ± 4.1	
14	165	18.453 ± 2.238	114.348 ± 14.083	6.20	1.0034	0.9550	38.55 ± 4.8	
17	155	21.943 ± 1.925	109.06 ± 12.482	4.97	0.9950	0.9555	*45.81 ± 4.22**	
18	155	16.66 ± 1.788	81.015 ± 9.528	4.86	0.9950	0.9555	35.37 ± 3.92	
19	150	14.449 ± 1.674	76.224 ± 9.451	5.28	0.9909	0.9554	30.98 ± 3.7	
20	150	19.035 ± 1.964	89.438 ± 10.576	4.70	0.9909	0.9555	40.13 ± 4.29	
21	150	19.246 ± 1.273	84.108 ± 10.157	4.37	0.9909	0.9554	40.54 ± 2.92	
22	150	15.624 ± 1.131	75.772 ± 9.028	4.85	0.9909	0.9555	33.4 ± 2.6	
23	150	15.353 ± 1.117	86.771 ± 11.62	5.65	0.9909	0.9555	32.84 ± 2.56	
24	150	17.133 ± 1.204	73.357 ± 12.197	4.28	0.9909	0.9555	36.44 ± 2.76	**37.37 ± 4.44**
Terrace T3i								
28	150	18.179 ± 1.314	73.916 ± 19.572	4.07	0.9909	0.9558	38.45 ± 2.98	**38.45 ± 2.98**
Terrace T2i								
29	140	17.35 ± 1.2	86.018 ± 10.346	4.96	0.9825	0.9558	37.13 ± 2.77	
30	140	15.679 ± 1.181	80.765 ± 10.841	5.15	0.9825	0.9558	33.78 ± 2.72	**35.45 ± 2.37**
Terrace T2d								
1	84	15.287 ± 0.561	84.65 ± 9.573	5.54	0.9367	0.9533	34.6 ± 1.6	
3	84	16.378 ± 0.586	102.963 ± 7.337	6.29	0.9367	0.9533	36.9 ± 1.68	
7	75	15.639 ± 0.547	91.353 ± 11.1	5.84	0.9295	0.9533	35.62 ± 1.6	
2	84	14.561 ± 1.702	91.357 ± 7.346	6.27	0.9367	0.9534	33.02 ± 3.97	
4	84	16.11 ± 1.857			0.9367	0.9534	36.34 ± 4.31	
5	84	16.315 ± 1.874	82.935 ± 6.668	5.08	0.9367	0.9533	36.77 ± 4.35	
6	80	15.919 ± 2.582	81.591 ± 8.387	5.13	0.9335	0.9533	36.06 ± 5.94	
8	75	14.984 ± 1.871	75.843 ± 14.617	5.06	0.9295	0.9534	34.2 ± 4.38	**35.44 ± 1.37**
Terrace T1								
50	30	7.253 ± 0.265	63.346 ± 7.857	8.73	0.8938	0.9534	17.52 ± 0.81	
51	30	4.576 ± 0.184	31.98 ± 5.048	6.99	0.8938	0.9532	11.08 ± 0.54	**14.30 ± 4.56**
52	30	15.679 ± 0.503	117.253 ± 14.841	7.48	0.8938	0.9534	37.02 ± 1.58	
			Average =	5.48 ± 1.07				**Average T2 35.53 ± 2.48**

§ Mean is average of ^{10}Be age, and error is standard deviation.
* Not included in average calculation.

Table 2. Amount and source of slip-rates along the faults of southern California as discussed in the text and plotted in Figure 9.

Fault	Slip-rate (mm/yr)	Time range	Reference
Geologic			
San Andreas Fault			
Wallace Creek (WC)	34 ± 3	3700 yrs	*Sieh and Jahns* [1984]
Pallet Creek (PC)	35 ± 7	500 yrs	*Salyards et al.* [1992]
Cajon Pass (CP)	24.5 ± 3.5	15 kyrs	*Weldon and Sieh* [1985]
Thousand Palms Oasis	4 ± 2	900 yrs	*Fumal et al.* [2002]
Indio	15.9 ± 3.4	35.5 kyrs	(this study)
	10 - 35	20 - 70 kyrs	*Keller et al.* [1982]
Mecca Hills	6.5 ± 1.5	34 kyrs	*Shifflett et al.* [2002]
Salt Creek	9 ± 2	900 yrs	*Williams* [1989]; *Sieh and Williams* [1990]
Imperial Fault Zone (IFZ)	15 -20	300 yrs	*Thomas and Rockwell* [1996]
West of San Andreas			
San Jacinto Fault	20	100 kyrs	*Kendrick et al.* [2002]
	6 - 23	50 kyrs	*Rockwell et al.* [1990]
	1 - 12	700 kyrs	*Sharp* [1981]
Elsinore Fault	4 - 6	600 kyrs	*Petersen and Wesnousky* [1994]
Newport-Inglewood Fault Zone (NIFZ)	1 - 3	-*	*Petersen and Wesnousky* [1994]
Coronado Bank Fault Zone (CBFZ)	2	-*	*Jennings* [1994]
San Diego Trough Fault Zone (SDTFZ)	1.5	-*	*Jennings* [1994]
San Clemente Fault	1 - 3	-*	*Jennings* [1994]
East of San Andreas			
Owens Valley Fault Zone (OVFZ)	2 - 4	4000 yrs	*Lee et al.* [2001]
Panamint Valley Fault Zone (PVFZ)	1 - 2	10 kyrs	*Hart et al.* [1989]
Death Valley Fault Zone (DVFZ)	2 - 4	-*	*Wesnousky* [1986]
Garlock Fault Zone (GFZ)	2 - 11	14 kyrs	*McGill and Sieh* [1993]
Lockhard Fault	1	-*	*Jennings* [1994]
Harper Fault Zone	1	20 kyrs	*Petersen and Wesnousky* [1994]
Blackwater Fault (BF)	2	20 kyrs	*Dokka and Travis* [1990]
Emerson Fault (EMF)	1	20 kyrs	*Dokka and Travis* [1990]
Calico Fault zone (CFZ)	1 - 2	20 kyrs	*Dokka and Travis* [1990]
Bullion Fault (BUF)	1	-*	*Jennings* [1994]
Pinto Mountain Fault (PMF)	1	5 - 20 Ma	*Wesnousky* [1986]
Plate Boundary (Nuvel - 1A)	52 ± 2	3.16 Ma	*Demets* [1995]; *Demets and Dixon* [1999]
Geodetic			
San Andreas Fault			
Southern SAF	23 ± 2	15 yrs	*Bennett et al.* [1996]
Southern SAF (VLBI)	26 ± 2		*Feigl et al.* [1993]
Salton Sea	23.3 ± 0.5	15 yrs	*Meade and Hager* [2005]
San Jacinto Fault	11.9 ± 1.2	15 yrs	*Meade and Hager* [2005]
	9 ± 2	10 yrs	*Bennett et al.* [1996]
Elsinore Fault	6 ± 2	15 yrs	*Bennett et al.* [1996]
Owens Valley Fault Zone (OVFZ)	2.1 ± 0.7	15 yrs	*Dixon et al.* [2003]
Plate Boundary	49 ± 3	15 yrs	*Bennett et al.* [1996]
Plate Boundary (VLBI)	47 ± 1		*Feigl et al.* [1993]

* Data not available.

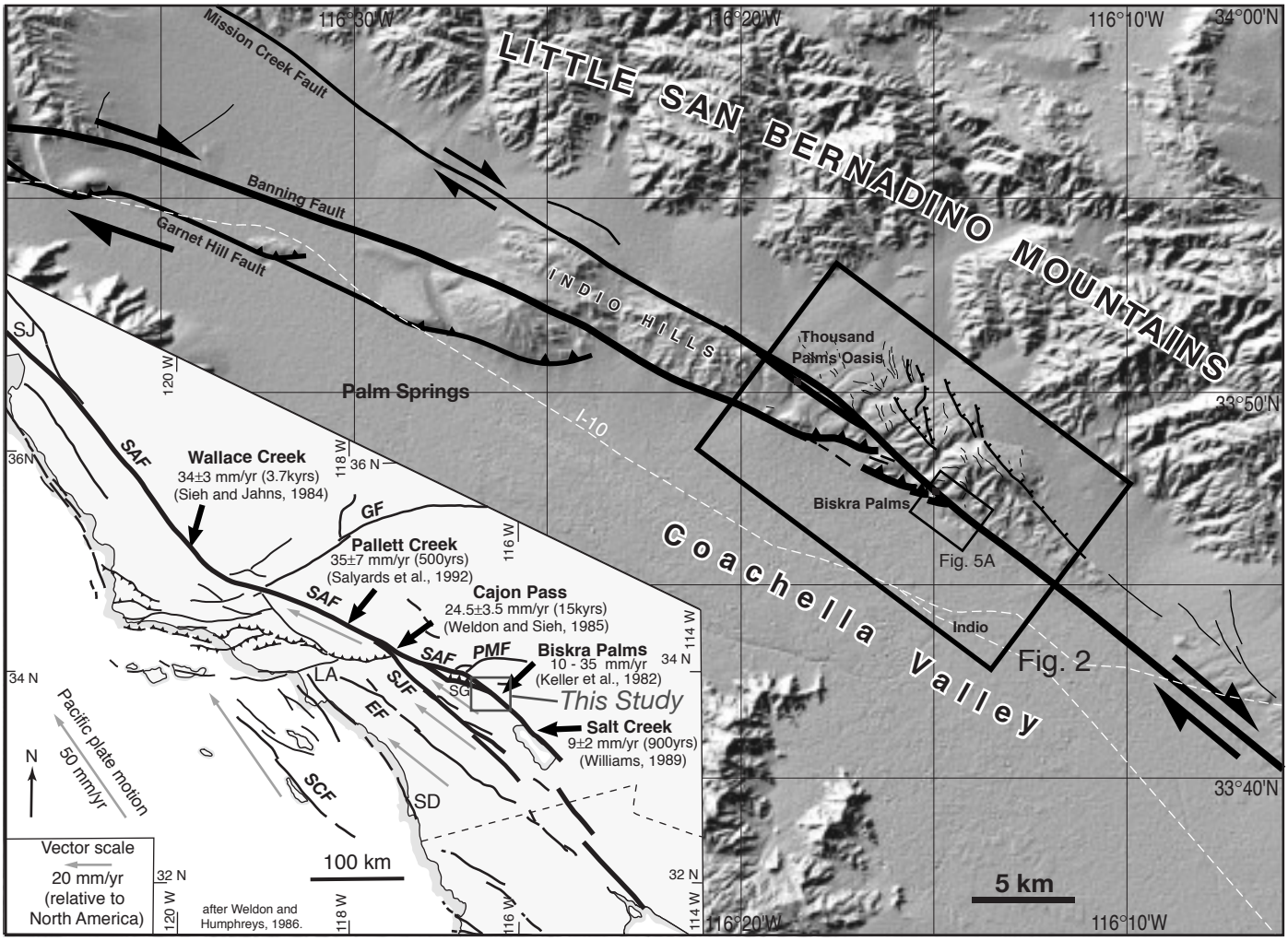
116°30'W
116°20'W
116°10'W
34°00'N
33°50'N
33°40'N
LITTLE SAN BERNADINO MOUNTAINS
Mission Creek Fault
Banning Fault
Garnet Hill Fault
INDIO HILLS
Thousand Palms Oasis
Palm Springs
I-10
Biskra Palms
Fig. 5A
Coachella Valley
Indio
Fig. 2
SJ
SAF
Wallace Creek
34±3 mm/yr (3.7kyrs)
(Sieh and Jahns, 1984)
GF
Pallett Creek
35±7 mm/yr (500yrs)
(Salyards et al., 1992)
Cajon Pass
24.5±3.5 mm/yr (15kyrs)
(Weldon and Sieh, 1985)
PMF
Biskra Palms
10 - 35 mm/yr
(Keller et al., 1982)
This Study
LA
SJF
EF
SG
Salt Creek
9±2 mm/yr (900yrs)
(Williams, 1989)
SCF
SD
N
Pacific plate motion
50 mm/yr
Vector scale
20 mm/yr
(relative to
North America)
100 km
after Weldon and
Humphreys, 1986.
5 km
36N
36 N
34 N
32 N
120 W
118 W
116 W
114 W

Figure 1


A
N
2 km

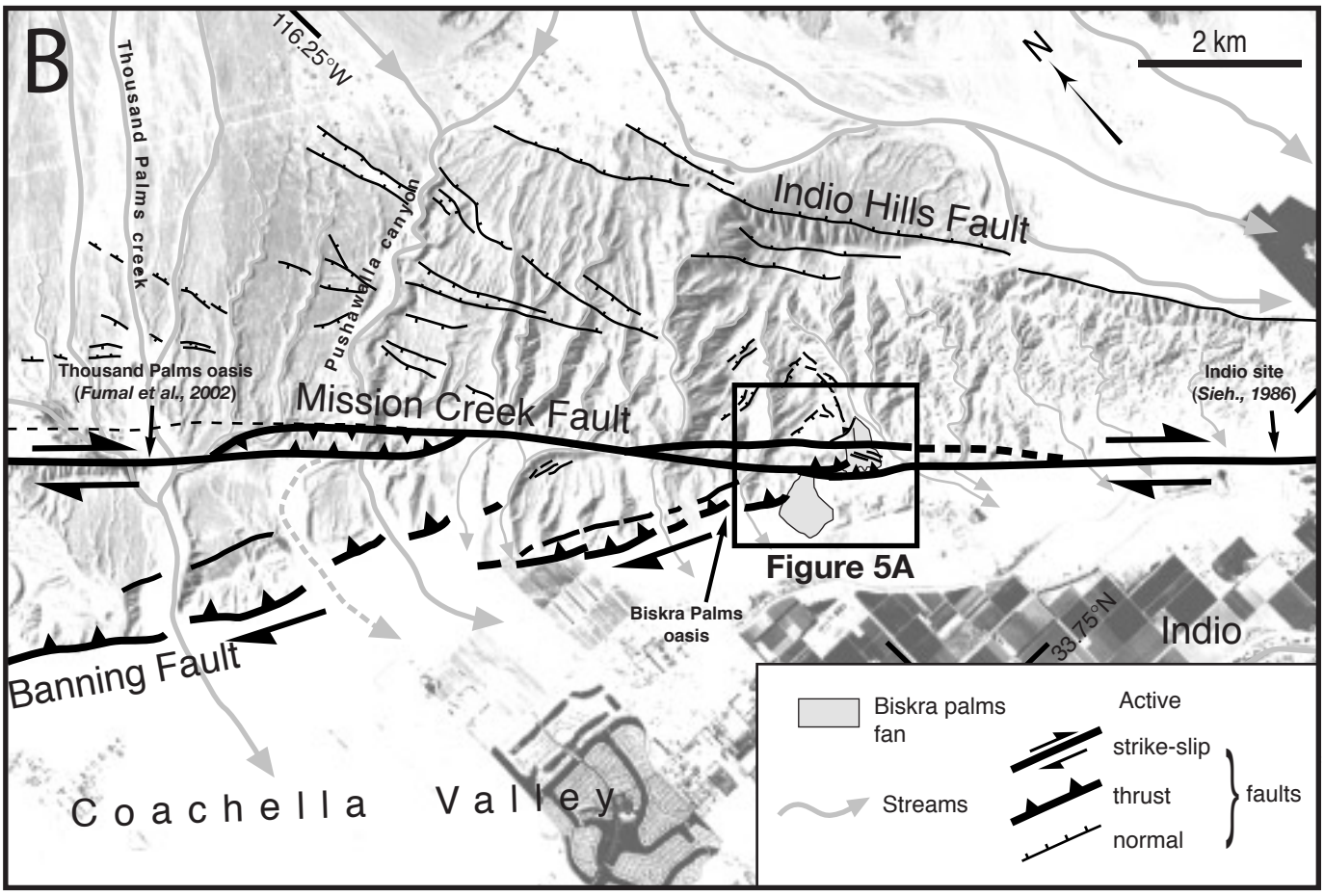
B
116.25°W
Thousand Palms creek
Pushawalla canyon
Indio Hills Fault
N
2 km
Thousand Palms oasis
(Fumal et al., 2002)
Mission Creek Fault
Indio site
(Sieh., 1986)
Figure 5A
Biskra Palms
oasis
33.75°N
Indio
Banning Fault
Coachella Valley
Biskra palms
fan
Streams
Active
strike-slip
thrust
normal
faults

Figure 2

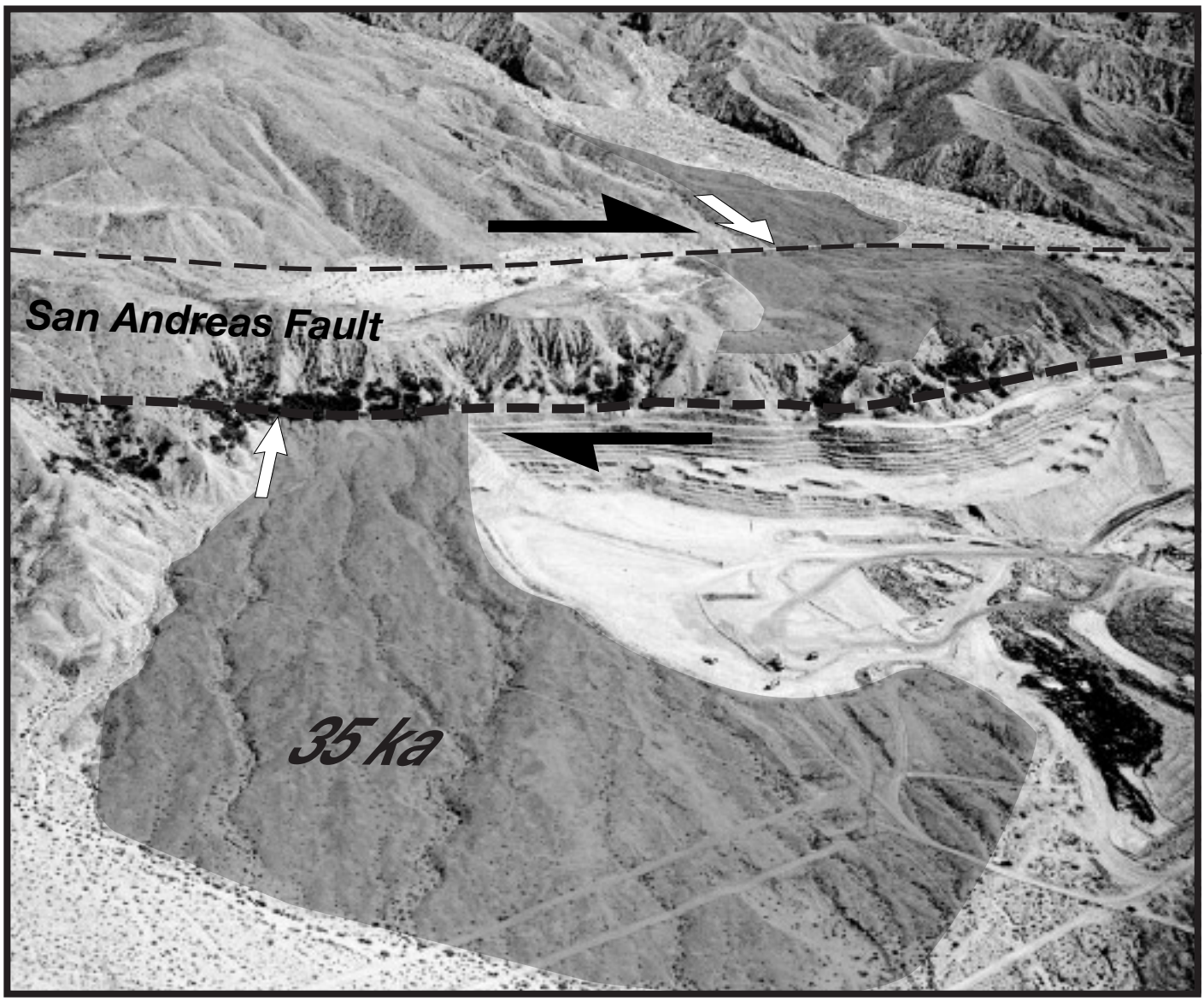

Figure 3

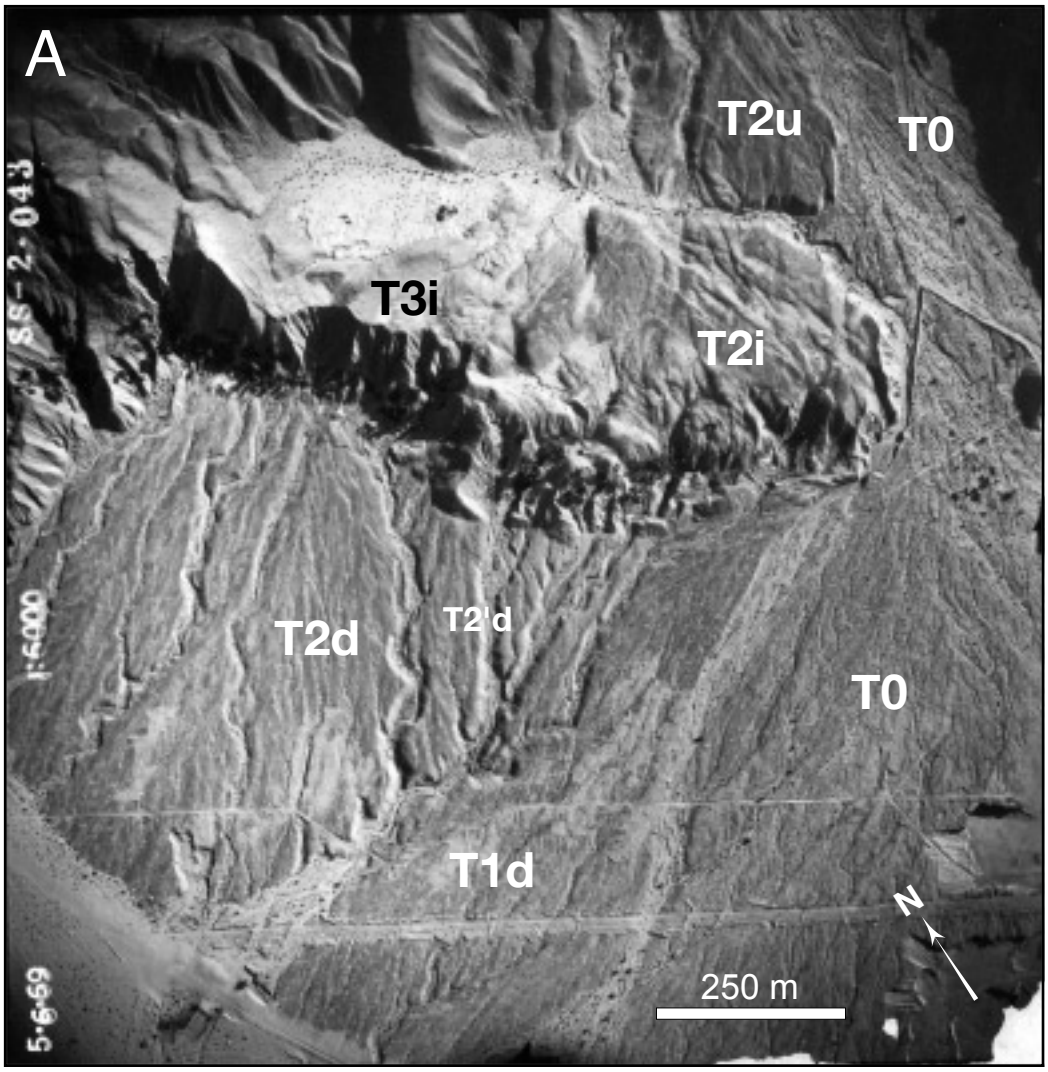

Figure 4

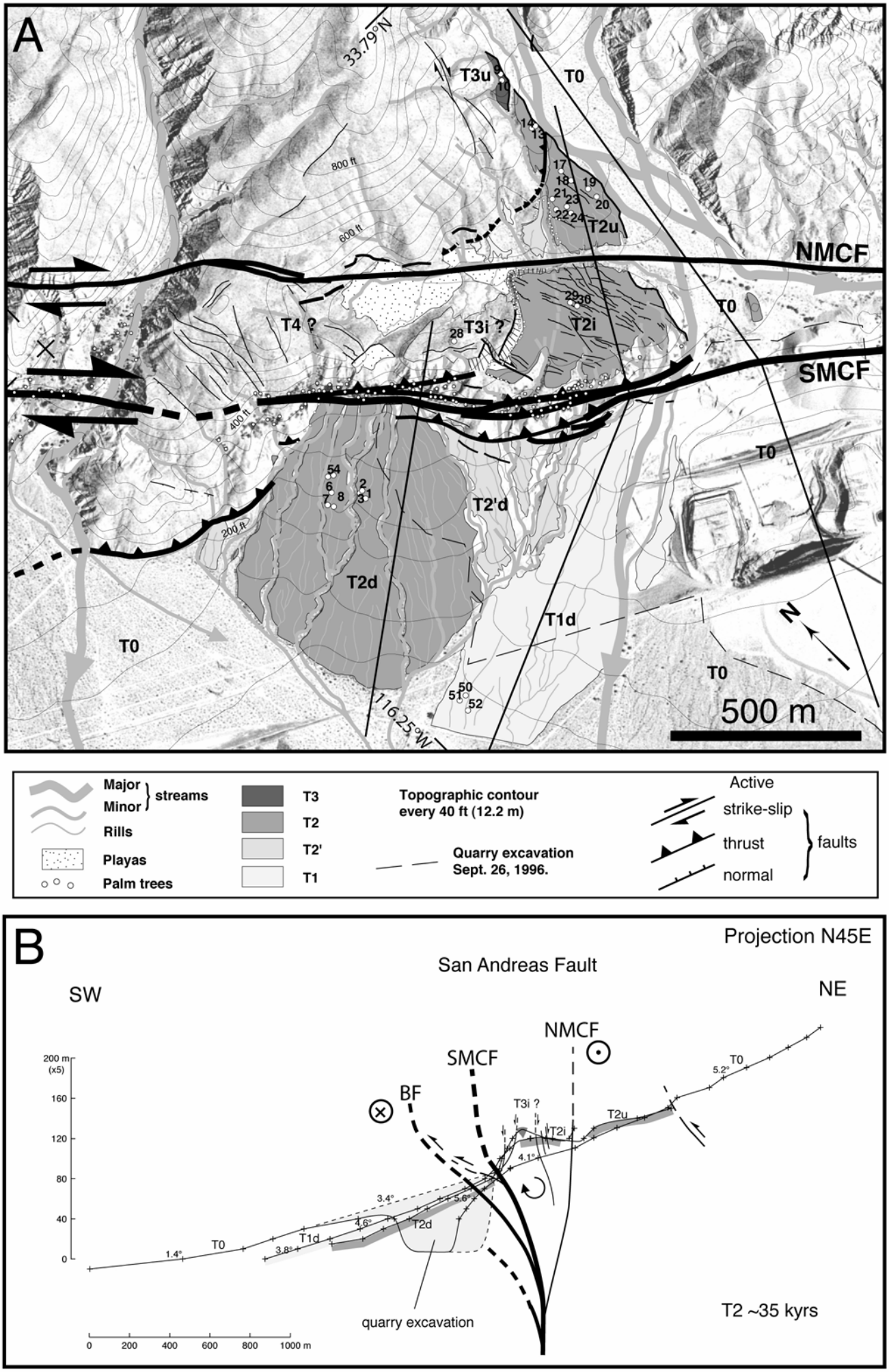
A
33.79°N
116.25°W
T3u
T0
T2u
NMCF
T4 ?
T3i ?
T2i
SMCF
T2'd
T2d
T1d
800 ft
600 ft
400 ft
200 ft
N
500 m
Major
Minor
streams
Rills
Playas
Palm trees
T3
T2
T2'
T1
Topographic contour every 40 ft (12.2 m)
Quarry excavation Sept. 26, 1996.
Active
strike-slip
thrust
normal
faults
B
Projection N45E
San Andreas Fault
SW
NE
NMCF
SMCF
BF
T3i ?
T2i
T2u
T0
T1d
T2d
quarry excavation
T2 ~35 kyrs
200 m (x5)
0
200
400
600
800
1000 m

Figure 5AB

Figure 6

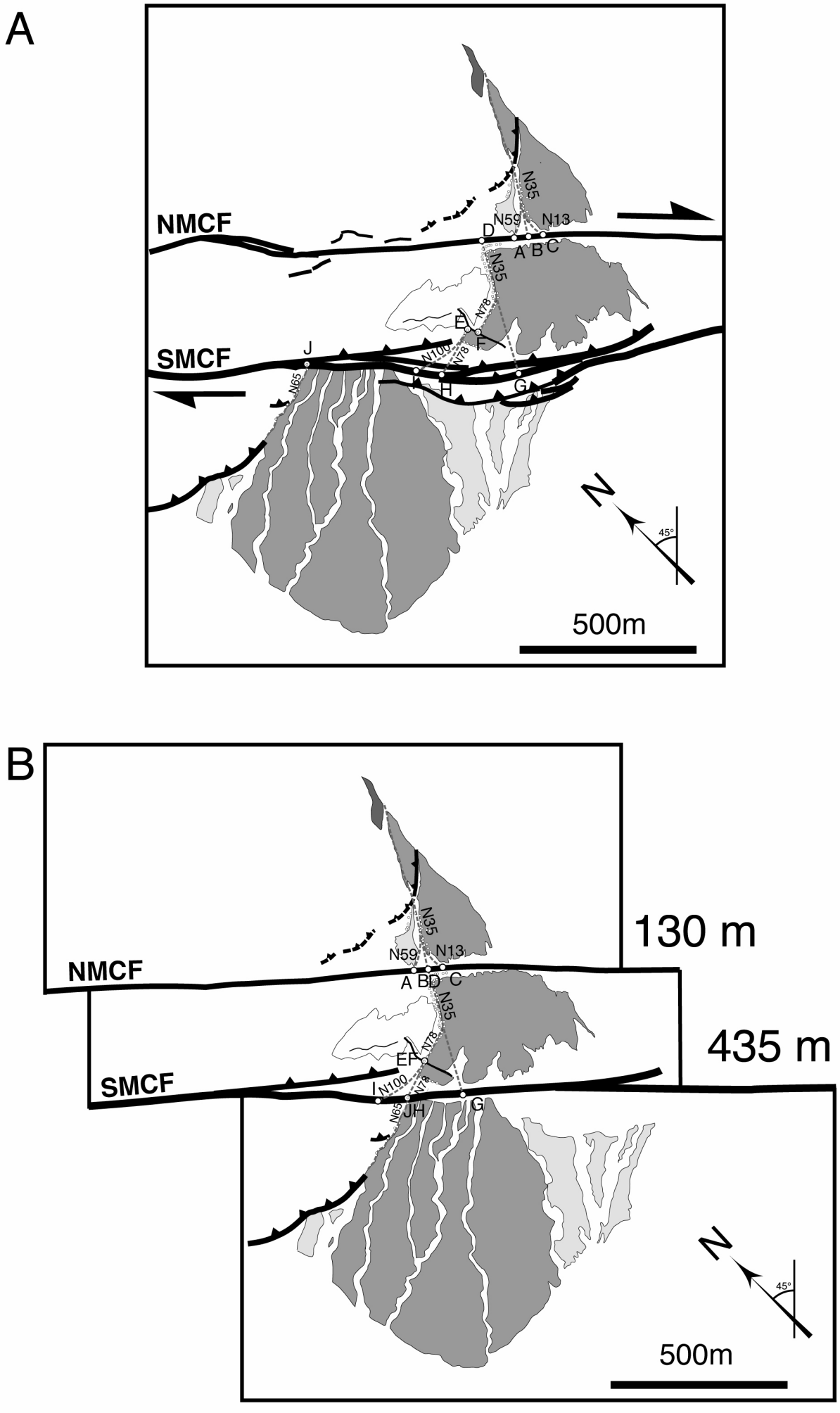
A
NMCF
SMCF
N35
N59
N13
D
A B C
N35
N78
E
F
J
N100
N78
N65
I
H
G
N
45°
500m
B
130 m
435 m
NMCF
SMCF
N35
N59
N13
A B D C
N35
N78
EF
N100
N78
N65
I
JH
G
N
45°
500m

Figure 7AB

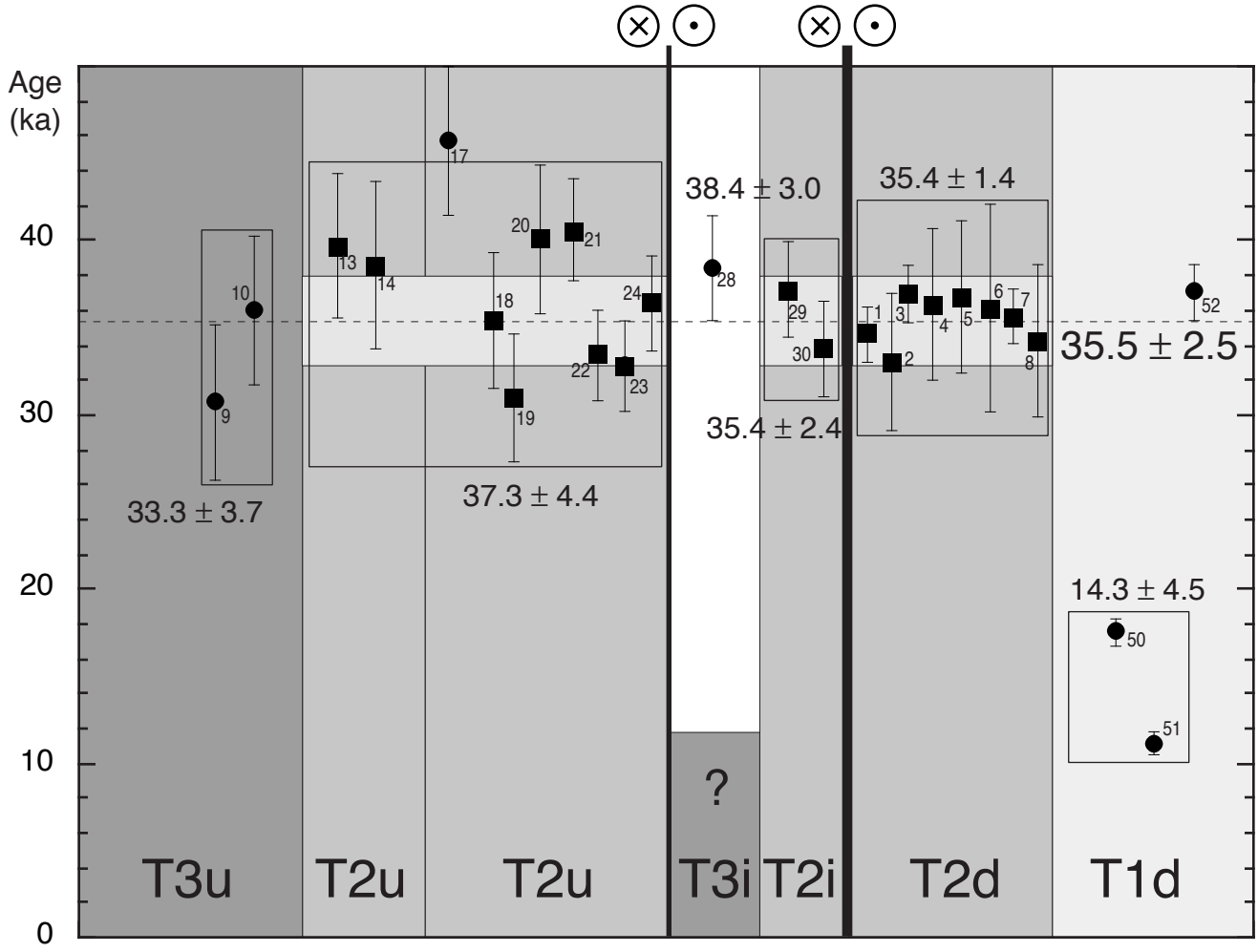
Age
(ka)
40
30
20
10
0
33.3 ± 3.7
37.3 ± 4.4
38.4 ± 3.0
35.4 ± 2.4
35.4 ± 1.4
35.5 ± 2.5
14.3 ± 4.5
?
T3u
T2u
T2u
T3i
T2i
T2d
T1d

Figure 8

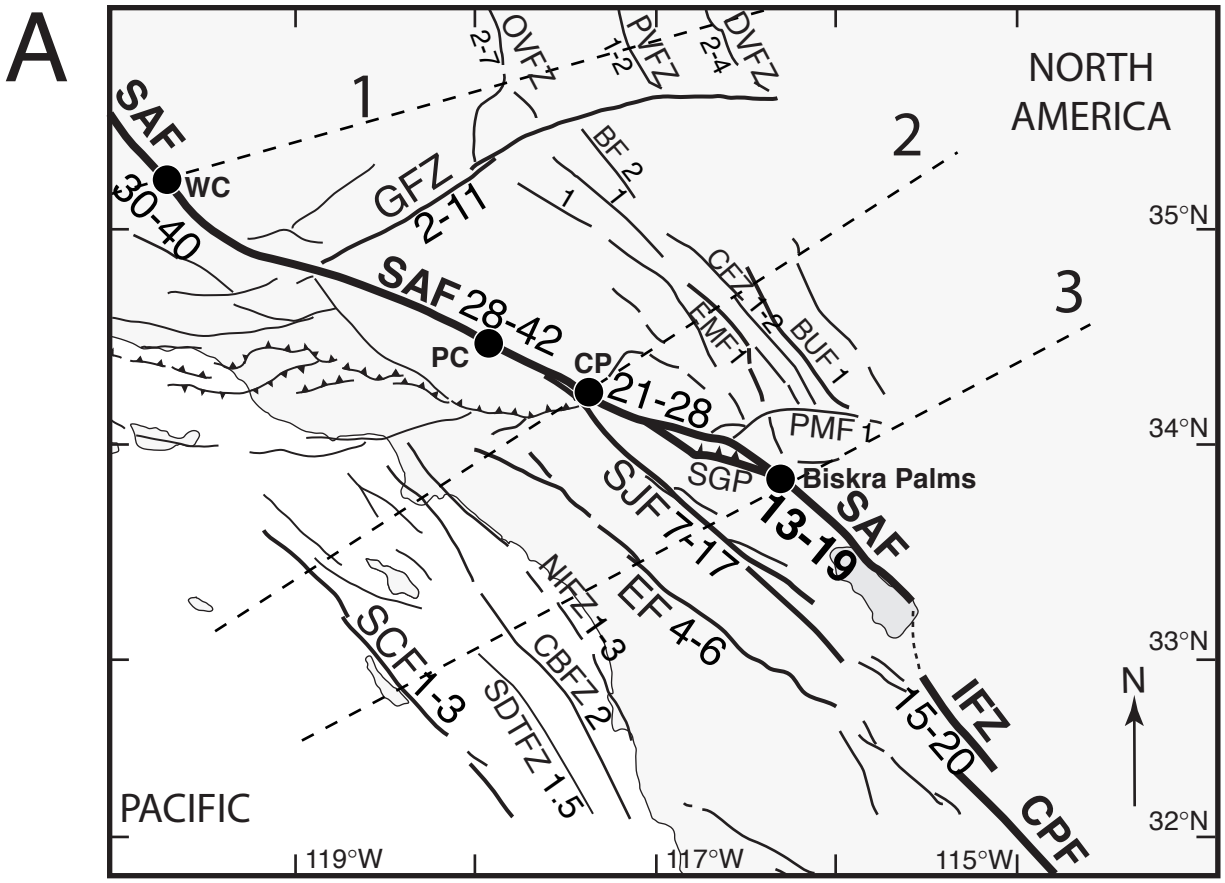
A
NORTH AMERICA
PACIFIC
SAF
WC
30-40
GFZ 2-11
SAF 28-42
PC
CP
21-28
SGP
Biskra Palms
SAF 13-19
SJF 7-17
EF 4-6
NIFZ 1-3
CBFZ 2
SDTFZ 1.5
SCF 1-3
IFZ 15-20
CPF
OVF 2-7
PVFZ 1-2
DVFZ 2-4
BF 2-1
CEF 1-2
EMF 1
BUF 1
PMF 1
1
2
3
35°N
34°N
33°N
32°N
119°W
117°W
115°W
N

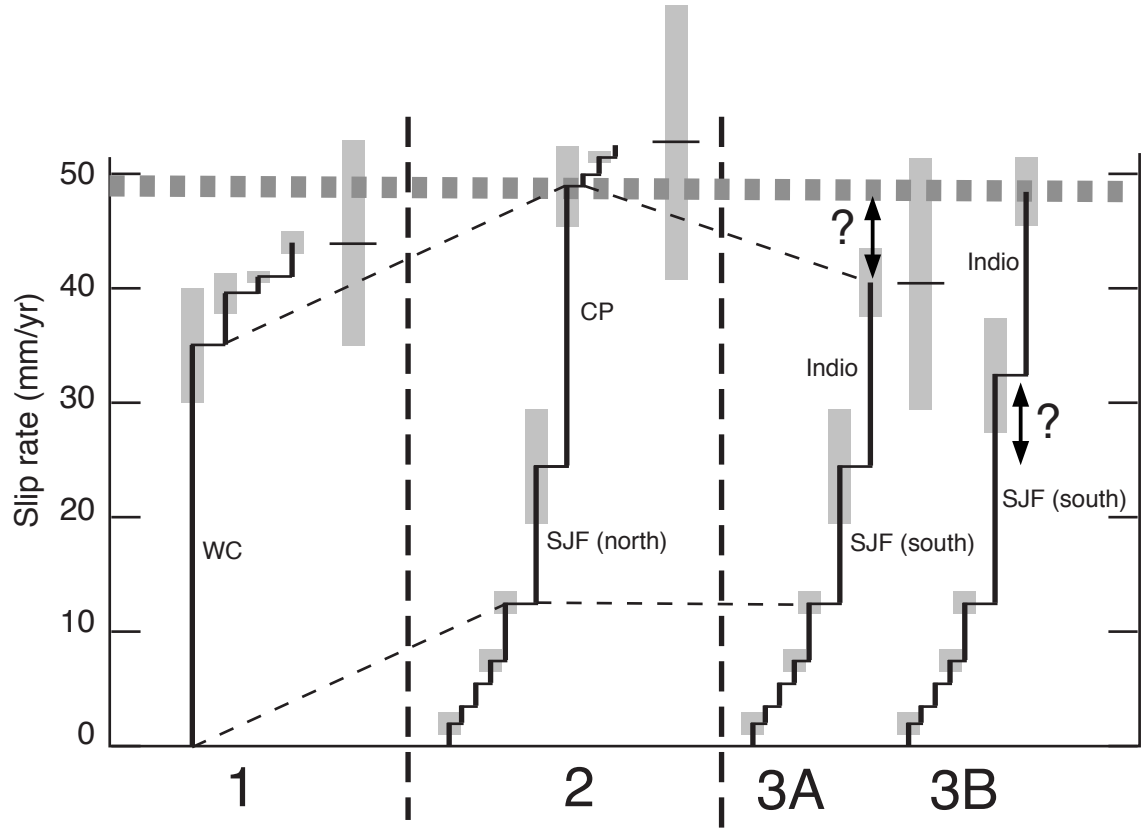
B
Slip rate (mm/yr)
50
40
30
20
10
0
WC
CP
SJF (north)
Indio
SJF (south)
Indio
SJF (south)
?
?
1
2
3A
3B

Figure 9